Computational Modeling of the Chlamydial Developmental Cycle Reveals a Potential Role for Asymmetric Division

Travis J. Chiarelli,[a] Nicole A. Grieshaber,[a] Cody Appa[a], Scott S. Grieshaber[a] #
[a]Department of Biological Sciences, University of Idaho, Moscow, Idaho, USA

Keywords: Chlamydia, differentiation, computational modeling

Running Title: Modeling of the Chlamydial Developmental Cycle

#Corresponding Author:
Scott S. Grieshaber
University of Idaho
Department of Biological Sciences
Moscow, ID 83844-3051
scottg@uidaho.edu
Ph: 352 575 0394

Abstract:

Chlamydia trachomatis is an obligate intracellular bacterium that progresses through an essential multi cell form developmental cycle. Infection of the host is initiated by the elementary body (EB). Once in the host, the EB cell differentiates into the non-infectious, but replication competent, reticulate body, or RB. After multiple rounds of replication, RBs undergo secondary differentiation eventually producing newly infectious EBs.

Here we generated paired cell type promoter reporter constructs and determined the kinetics of the activities of the *euo*, *hctA* and *hctB* promoters. The paired constructs revealed that the developmental cycle produces at least three phenotypically distinct cell types; the RB (*euo*prom+), IB (intermediate body, *hctA*prom+) and EB (*hctB*prom+). The kinetic data from the three dual promoter constructs, was used to generate two computational agent-based models to reproduce the chlamydial developmental cycle. Both models simulated EB germination, RB amplification, IB formation and EB production but differed in the mechanism that generated the IB. The Direct Conversion and the Asymmetric Production models predicted different behaviors for the RB population which were experimentally testable. In agreement with the Asymmetric Production model, RBs acted as stem cells after the initial amplification stage, producing one IB and self-renewing after every division. We also demonstrated that IBs are a transient cell population, maturing directly into EBs after formation without the need for cell division. The culmination of these results suggests that the developmental cycle can be described by a four-stage model, EB germination, RB amplification/maturation, IB production, and EB formation.

Importance:

Chlamydia trachomatis is an obligate intracellular bacterial pathogen responsible for both ocular and sexually transmitted infections. All *Chlamydiae* are reliant on a complex developmental cycle, consisting of both infectious and non-infectious cell forms. The EB cell form initiates infection, whereas the RB cell replicates. The infectious cycle requires both cell types as RB replication increases the cell population while EB formation disseminates the infection to new hosts.

The mechanisms of RB to EB development are largely unknown. Here, we developed unique dual promoter reporters and used live cell imaging and confocal microscopy to visualize the cycle at the single cell and kinetic level. These data were used to develop and test two agent-based models, simulating either direct conversion of RBs to EBs or production of EBs via asymmetric RB division.

Our results suggest that RBs mature into a stem cell-like population producing intermediate cell forms through asymmetric division, followed by maturation of the intermediate cell type into the infectious EB. Ultimately a more complete mechanistic understanding of the developmental cycle will lead to novel therapeutics targeting cell type development to eliminate chlamydial dissemination.

Introduction

Chlamydiae are obligate intracellular bacterial parasites that cause an array of diseases in both humans and animals. *Chlamydia trachomatis*, a human-adapted pathogen, is the leading global cause of bacterial sexually acquired infections and preventable blindness. In 2019, the CDC reported 1.8M *C. trachomatis* infections within the United States alone, with the most recent reports indicating that rates increased 10.0% in women and 32.1% in men from 2015-19 (1, 2). This increase in infection rates has been reported across all racial/ethnic groups and affects all age groups (2).

Chlamydial growth and development has classically been characterized as a biphasic cycle, consisting of two primary cell forms: the elementary and reticulate body (3). These cell forms maintain a division of labor throughout the infectious cycle and are essential for chlamydial proliferation. The elementary body (EB) is the infectious cell form and initiates host cell invasion by pathogen-mediated endocytosis (4). The EB cell form is non-replicative and the chromosome is tightly compacted by nucleoid associated proteins (5, 6). Upon entry into the host, the EB undergoes large transcriptional and phenotypic changes, maturing into the reticulate body (RB) in a process that takes up to 12 hours for serovar L2 (7, 8). The RB is replication competent but non-infectious and must re-differentiate back into the EB to disseminate the infection to new host cells (9, 10).

Electron micrographs have also shown the presence of a transitory cell form, termed the intermediate body (IB). IBs are present beginning between 20 and 24 hpi for serovar L2 and are characterized by a semi-condensed nucleoid similar to the EB, but are significantly larger giving them a target-like appearance (8, 11). Due to the presence of the IB and its appearance as a transitory form, it is currently hypothesized that a subset of RBs undergo large morphological changes to convert directly into EBs.

We previously reported the development of a live-cell reporter system to follow the chlamydial cycle in real time at the single inclusion level. A suite of different gene promoters were designed to drive the expression of fluorescent proteins in order to follow RB growth and EB development. These kinetic data suggested that the promoters fell into three temporal categories exemplified by the activity of the *euo*, *hctA* and *hctB* promoters (11)

In this study, paired promoter reporter constructs were developed to determine the temporal and spatial relationships between the activities of the *euo*, *hctA* and *hctB* promoters at the kinetic and single cell level. Based on the expression kinetics of these reporters and their kinetic relationships to each other, computational agent-based models were created to best represent the developmental cycle. Two models were developed to explain the data: a RB to IB direct conversion model and an asymmetric division/production model. The outputs of simulations from these models were compared to experimental data to determine which mechanism was best supported. Our model and data suggest a novel RB amplification/maturation step where the RB initially divides symmetrically to produce two RBs and increase RB numbers, followed by maturation of the RB to an asymmetrically dividing cell that produces one IB while regenerating the RB. Our data also support the direct maturation of the IB cell type into the EB without the need for cell division.

Results:

Development of dual fluorescent cell reporter constructs to determine cell type gene expression during the developmental cycle. We previously reported the use of promoter reporter constructs that were expressed at different stages of the chlamydial developmental cycle (11). Fluorescence from the *euo*prom-clover construct was first detected at ~14 hours post infection (hpi) and demonstrated a short

exponential phase, followed by an expression plateau at ~24 hpi (11). Imaging of the *hctA*prom-clover construct revealed that the Clover signal could first be detected at ~18 hpi and continued to increase until cell lysis (11). Additionally, we noted that *hctB*prom-Clover expression was initiated at ~ 22 hpi, ~4 hours later than *hctA*prom, and also increased linearly until cell lysis (11)

Here, we extended these studies by combining these promoters in pairs on the same plasmid. In addition, the LVA degradation tag was used to target fluorescence proteins for degradation to increase temporal resolution. To visualize expression kinetics and expression relationships between these cell type promoter reporters at the single inclusion and single cell level, we constructed three dual fluorescent developmental gene expression reporter strains, hctAprom-euoprom, hctBprom-hctAprom, and hctBprom-euoprom. For the hctAprom-euoprom (AMELVA) construct, the euo promoter was used to drive the expression of the green fluorescent protein variant, mNeonGreen (mNG) (12) fused in frame to the LVA protein degradation tag which reduced the fluorescent half-life to ~30 min (13), and the hctA promoter was used to drive the expression of the red fluorescent protein mKate2 (14) (Fig. S1A). The hctBprom-euoprom (BMELVA) dual reporter construct was created by replacing hctAprom in AMELVA with hctBprom to drive mKate2 expression (Fig. S1B). Lastly, to create the hctBprom-hctAprom (BMALVA) dual reporter, the hctA promoter was used to drive mNG(LVA) and the hctB promoter was used to drive mKate2 expression (Fig. S1C). Each construct was transformed into Chlamydia trachomatis L2, creating the L2-AMELVA, L2-BMELVA, and L2-BMALVA reporter strains (Table 1), and compared to our previously reported dual promoter strain L2-hctBprom_mKate2-euoprom_clover (L2-BMEC) (11). To determine the relationships between the promoter reporters, we investigated the expression of each paired reporter at the single chlamydial cell level by confocal microscopy (Fig. 1A), and the single inclusion kinetic level by live cell imaging (Fig. 1B). For confocal imaging, host cells were infected with each strain for 24 hours followed by fixation. All L2-BMEC chlamydial cells showed some level of green fluorescence, suggesting that all cells expressed from the euoprom-clover construct at some point during the developmental cycle (Fig. 1A, L2-BMEC). However, confocal microscopy of the new strains using the short half life mNG(LVA) fluorescent reporter revealed that the three promoters were active exclusively from one another (Fig. 1A). The euoprom-mNG(LVA) signal from the L2-AMELVA strain was present in large RB sized cells, while hctAprom-mKate2 was active in a subset of large and small cells but in a population distinct from euoprom+ cells (Fig. 1A, L2-AMELVA). The euoprom-mNG(LVA) signal from L2-BMELVA was also present in large cells only, while the hctBprom-mKate2 signal was present in small cells and in an entirely distinct population (Fig. 1A, BMELVA). In the L2-BMALVA infected cells, hctAprom-mNG(LVA) expression was visible in large and small cells while hctBprom-mKate2 signal was detected in small cells. Again, the two promoter reporters were active in distinct, non-overlapping populations (Fig. 1A, L2-BMALVA). Occasionally, we saw paired hctAprom expressing cells but we do not know the origin or fate of these cells as these are static images of a dynamic environment.

We quantified the expression of the paired fluorescent reporters at the single cell level in four individual inclusions for each strain. The TrackMate plugin in FIJI (15) was used to identify GFP and RFP expressing cells and record the fluorescent signal for each reporter from entire confocal z stacks encompassing each inclusion. The paired fluorescent signals for each cell were plotted, the RFP on the y-axis and the GFP signal on the x-axis (Fig. 1A). For the L2-BMEC strain expressing the stable GFP protein, Clover, driven by the euo promoter, both green and red cells had Clover signal demonstrating that both cell types expressed Clover from the euo promoter at some point during the developmental cycle of that cell. In contrast, the red and green expressing Chlamydia cells of the L2-BMELVA strain

which expresses a short half life fluorescent protein from the euo promoter,are distinct populations with minimal overlap. The same was seen for the L2-AMELVA and L2-BMALVA infections; the red expressing cells had minimal green signal (AMELVA) and the green expressing cells had minimal red signal (BMALVA). Together, these data demonstrate that the three promoters are active in distinct subpopulations of chlamydial cells.

In addition to the confocal images the kinetics of each promoter was determined at the single inclusion level using live-cell microscopy. Host cells were infected with each strain and imaged for both GFP and RFP from 10 hpi until 50 hpi at 30 minute intervals. *Euo*prom-mNG(LVA) signal from L2-AMELVA was first detected at ~14 hpi and increased exponentially until ~26 hpi after which time the signal reached a plateau that was maintained for the duration of the infection (Fig. 1B, L2-AMELVA). The *hctA*prom(mKate2) signal was first detectable at ~18 hpi with an exponential increase in expression until 28 hpi, followed by a linear increase until the end of the experiment at 50 hpi (Fig. 1B, L2-AMELVA). Like L2-AMELVA, the *euo*prom-mNG(LVA) signal for L2-BMELVA followed the same kinetics with an early exponential increase followed by a signal plateau (Fig. 1B, L2-BMELVA). The *hctB*prom signal in these inclusions became detectable at ~24 hpi and increased exponentially until ~34 hpi. After this brief exponential phase, *hctB*prom(mKate2) signal increased at a linear rate until the end of the experiment (Fig. 1B, L2-BMELVA). Live-cell kinetics of L2-BMALVA showed that *hctA*prom-mNG(LVA) activity initiated around 18 hpi, however expression approached steady state kinetics and did not accumulate (Fig. 1B, L2-BMALVA). *HctB*prom(mKate2) demonstrated the same kinetics as the L2-BMELVA strain (Fig. 1B). The short half-life of the LVA tagged mNG allowed for spatial and kinetic resolution of three cell types. These results demonstrate that chlamydial cells follow a temporal gene expression program resulting in three distinct cell forms. The RB cell activity expresses from the euoprom, while the EB cell expresses from the hctBprom. The observation that *hctA*prom was temporarily active after *euo*prom and before *hctB*prom, and the observation that *hctA*prom is active in a distinct cell population from *euo*prom+ cells and *hctB*prom+ cells suggest that *hctA*prom is active in the IB cell population. Overall, these data suggest that the developmental cycle can be represented by three phenotypically distinct cell types; RB cells (*euo*prom+), IB cells (*hctA*prom+) and EB cells (*hctB*prom+).

Live-cell imaging also revealed the interrelated kinetics of the activity of these promoters. The kinetic data from each individual inclusion of both L2-AMELVA (Fig. 2A) and L2-BMELVA (Fig. 2B) revealed that there was significant heterogeneity in the maximal expression level of the *euo*prom plateau. Interestingly, the variation in *euo*prom expression from the paired expression constructs correlated with the rates of *hct*Aprom (L2-AMELVA) and *hctB*prom (L2-BMELVA) signal accumulation, i.e. inclusions exhibiting high *euo*prom plateaus had steeper slopes for *hctA*prom and *hctB*prom signal accumulation, while lower *euo*prom signal correlated with a lower rate of *hct*Aprom and *hctB*prom signal accumulation (Fig. 2A and B). When the *hctA*prom and *hctB*prom signals were normalized to the *euo*prom signal plateau for each inclusion, the variation in the slopes of *hctA*prom(mKate2) and *hctB*prom(mKate2) accumulation was dramatically reduced (Fig. 2A and B). This variability in the maximum expression levels of *euo*prom suggested that each inclusion contained differing numbers of RB (*euo*prom+) cells during the plateau phase, which in turn lead to the varying IB (*hctA*prom) and EB (*hctB*prom) accumulation rates.

To test whether the differing plateau signal of *euo*prom expression was due to differing RB numbers, cells were infected with L2-BMELVA at an MOI of ~0.1 and fixed and stained with DAPI every 2 hours from 14 to 48 hpi. Infected cells were imaged by 3D confocal microscopy and cell type

196 quantification was carried out using an automated cell counting workflow using the open-source
197 software FIJI and the TrackMate plugin to count individual *Chlamydia* based on fluorescent reporter
198 intensity (12). These experiments revealed that RB (*euo*prom+) cells increased in number from 14 hpi
199 until 26 hpi, reaching an average of ~30/inclusion (Fig. 2C). After this time point, the average number of
200 RBs was unchanged. However, it was clear that the maximum number of RBs in each inclusion varied
201 significantly with some inclusions having as few as one *euo*prom+ cell while others had as many as 59
202 RBs/inclusion during this plateau phase (26-48 hpi) (Fig. 2C). A similar time course was carried out for
203 cells infected with L2-BMALVA, with similar results. IBs (*hctA*prom+) cells increased in number from 17
204 hpi until reaching a maximum at 32 hpi, after which the average of IBs/inclusion remained steady (Fig.
205 2D). Again, similar to the *euo*prom+ cells, the number of *hctA*prom+ cells was significantly different on a
206 per inclusion basis with some inclusions having as few as a single *hctA*prom+ cell while others had as
207 many as 65 during the plateau phase (Fig. 2D). These data suggest that the chlamydial developmental
208 cycle produces significant heterogeneity between inclusions, but that despite this heterogeneity, each
209 inclusion produces similar kinetic relationships between cell types.
210
211 **Modeling the chlamydial developmental cycle.** Dissecting the mechanisms that control the
212 developmental cycle in *Chlamydia* has in part been inhibited by the reliance on population-based
213 studies. Using the individual inclusion kinetic data and individual cell expression data generated from
214 L2-AMELVA, L2-BMELVA and L2-BMALVA, we divided the cycle into discrete steps: EB germination,
215 RB amplification, IB formation, and EB maturation. To explore potential mechanisms involved in these
216 steps, two agent based models (ABMs) were developed to describe the developmental cycle using the
217 Python-based bacterial growth simulation platform, Cellmodeller (13). Euo, HctA and HctB protein
218 expression was simulated in each cell type over time for both models (Sup model). Additionally,
219 germination was set at 10 hpi as the first replication event has been previously reported at this time
220 point (11, 14), and agrees well with initiation of *euo* promoter expression (Fig. 1 and 2) (11). The two
221 models differed in the mechanism controlling RB amplification and IB formation. The Asymmetric
222 Production model used a RB maturation mechanism where early RBs (designated the RB_R) replicate to
223 produce two identical RB_R daughter cells, resulting in RB_R number amplification. This step is followed
224 by a RB_R maturation phase where the RB_R matures over time into a cell form that undergoes
225 asymmetric cell division (designated the RB_E), producing one RB_E daughter cell and one IB daughter
226 cell. The Direct Conversion model used a stochastic direct conversion mechanism where early RBs
227 replicate resulting in RB number amplification followed by an increase in the chance that an RB
228 transitions into the IB state. This stochastic chance of conversion increases over time before reaching a
229 maintenance state where RB amplification and conversion rates are matched (Sup model, SM1). Both
230 models reproduced the developmental kinetics that were observed using L2-AMELVA, L2-BMELVA
231 and L2-BMALVA (Fig. 3A and Fig. 1 and 2). However, the stochastic model needed to be constrained
232 to match the experimental data. When conversion became greater than RB replication, RB numbers
233 dropped to extinction. Conversely, when the RB replication rate remained higher than the conversion
234 rate, RBs quickly outnumbered EBs (Fig. 3B).
235 Although both models could produce similar kinetics at the population level, simulations of individual
236 inclusions demonstrated large kinetic differences. For the Asymmetric Production model, simulated
237 inclusions with high RB numbers had corresponding high EB production rates, while inclusions with low
238 RB numbers had corresponding low EB production rates. The EB production rate for each inclusion,
239 regardless of RB numbers, was linear while the RB population numbers remained unchanged over time

(Fig. 3C: Asymmetric Production). The kinetics for the Direct Conversion model had similar trends, however there were obvious runs of over and under amplification/conversion for both RB and EB numbers in the individual inclusion simulations, demonstrating that the stochastic mechanism can reliably reproduce the observed data only on the population level. These simulations suggest that the Asymmetric Production model is a better match for the observed developmental kinetics.

Steady state vs stem cell population. The Asymmetric Production model predicts that after amplification the RBs act as a stem cell population, producing IBs while self-renewing after every division (Mov. S1). In contrast, the Direct Conversion model predicts that RBs convert directly into IBs and are subsequently replaced by a dividing RB population, producing a steady state of RBs (Mov. S2). To determine which of these phenotypes the RB is exhibiting, live-cell imaging at high resolution (40X objective) of cells infected with L2-BMELVA was used to follow RB behavior. Cells infected with L2-BMEVLA were imaged for *euo*prom and *hctB*prom expression every 15 minutes starting at 24 hpi until 60 hpi. We imaged from 24 hpi until 60 hpi as this covers the end of the RB amplification stage until the end of the cycle. Imaging revealed that the number of RBs (*euo*prom+) per inclusion remained roughly the same throughout the experiment (Fig. 4A and Mov. S3). The RBs in each inclusion were easily tracked from one time point to the next and did not disappear while new RBs appeared. We also observed two binary divisions (RB amplification events) occurring between 26 hpi and 31 hpi (Fig. 4A, #3a and b, #5a and b, and Mov. S3). These newly formed RBs also remained trackable within the inclusion for the remainder of the experiment. These observations are consistent with stem cell-like behavior of the RBs after amplification.

Both models predicted that the IB cell type is maintained at steady state, i.e IBs mature into EBs and new IBs replace the maturing cells. To investigate the dynamics of the IB population, the L2-BMALVA strain was imaged from 24 hpi until 60 hpi at 15 min intervals. The dynamics of the IBs (*hctA*prom+ cells) resembled steady state kinetics; *hctA*prom+ cells would disappear while new *hctA*prom+ cells would appear (Fig. 4B, Mov. S4).

Together these data strongly support the Asymmetric Production model that predicts that RB numbers are amplified between 12 hpi and 28 hpi followed by a stem cell like behavior, producing one IB at division. In contrast, the IBs behave as a steady state population where, once formed, the IBs are converted directly into EBs.

The role of cell division on the RB population. Simulations of the two competing ABMs predicted different developmental outcomes if cell division was inhibited. The Asymmetric Production model predicted that RBs produce IBs only at division. Therefore, an immediate block in the formation of new IBs would occur but RB numbers would remain unaffected if replication was inhibited at 30 hpi (Fig. 5A). In contrast, the Direct Conversion model predicted that RB numbers would drop overtime if cell division was inhibited at 30 hpi, eventually disappearing as the RBs converted into IBs but were not replaced by further RB replication (Fig. 5B). To test these predictions experimentally, two cell replication inhibitors were used, penicillin (Pen) and ciprofloxacin (Cip). *Chlamydia* does not contain a peptidoglycan cell wall and instead uses peptidoglycan in septum formation, therefore Pen treatment of *Chlamydia* inhibits cell division (15). Ciprofloxacin prevents bacterial DNA replication by inhibiting topoisomerases and DNA-gyrase (16). Cells were infected with L2-BMELVA and >20 inclusions per treatment were imaged using a 60X 1.4 NA objective. Individual inclusions were imaged at multiple z planes to visualize and quantify all the RBs in the inclusion. Images were collected from the live

284 cultures at antibiotic treatment (30 hpi) and 10 hours later (40 hpi) (Fig. 5C and D). The number of
285 *euo*prom+ cells (RBs) was quantified on a per-inclusion basis. The same inclusions were quantified at
286 each time point. Consistent with the confocal time-series experiment, there was a large variation in the
287 number of RBs in individual inclusions, ranging from a single RB to greater than 50 RBs (Fig. 5C).
288 However, the number of RBs per inclusion remained essentially constant between the 30 hpi and 40
289 hpi timepoints (Fig. 5C). The mean ratio of RBs at 30 hpi and 40 hpi per inclusion was 1.27±0.28 for
290 untreated, 1.18±0.24 for Pen treated and 1.51±0.35 for Cip treated (Fig. 5D). There was an increase in
291 RB numbers in each inclusion when treated with Cip, but never more than double. We speculate that
292 although Cip treatment inhibited initiation of DNA replication, it did not significantly impact the
293 continuation of DNA replication and allowed cell division to finish in RBs that had already initiated DNA
294 synthesis. This is in agreement with our published data demonstrating that RBs are undergoing
295 continuous DNA replication as indicated by a replication index of 1.5 (17). This index is a ratio of
296 sequencing coverage near the origin of replication vs coverage near the terminus and represents the
297 growth rate of the population. An RB replication index of 1.5 demonstrates the presence of partially
298 replicated chromosomes (17)
299 To confirm that chlamydial DNA replication was inhibited by Cip, digital droplet (ddPCR) was
300 performed on L2-BMELVA infected samples treated with either Cip, Pen, or mock at 30 hpi. Host
301 monolayers were harvested every 4 h from 26-54 hpi. As previously reported, genome copy number
302 continued to increase in the Pen treated samples (11, 18). There was however, a large reduction in
303 genome copy accumulation after Cip treatment when compared to the mock and Pen treated samples
304 (Fig. S2B).
305
306 **The role of cell division on the IB population and EB production**. Simulations of the two competing
307 ABMs also predicted different developmental outcomes in the IB population if cell division was inhibited.
308 The Asymmetric Production model produces IBs only at division, therefore blocking cell division at 30
309 hpi predicted an immediate block in the formation of new IBs leading to an immediate halt in the
310 increase in IB gene expression (Fig. 6A, Asymmetric Production). In contrast, after replication was
311 inhibited, the Direct Conversion model predicted that IB gene expression would continue to increase
312 over a 12 hour period as the RBs converted into IBs, at which point IB gene expression would halt as
313 IBs could not be replenished by RB cell division (Fig. 6A, Direct Conversion).
314 To test these predictions experimentally, cell replication was inhibited with Pen, Cip or
315 genetically by overexpression of FtsI. Penicillin-binding proteins (PBPs) are a suite of enzymes
316 involved in peptidoglycan synthesis and cell division (22). Both PBP2 and PBP3 are (D,D)-
317 transpeptidases that mediate the formation of peptidoglycan. In *Escherichia coli,* PBP2 is required for
318 cell shape and stability, whereas PBP3 is involved in cell division (23). When overexpressed in *E. coli*,
319 PBP2 and PBP3 have been shown to induce lysis in dividing cells (24,25). However, as Chlamydia
320 does not contain a peptidoglycan cell wall, PBP2 and PBP3 have both been co-opted for use in
321 septation (26). Therefore, we overexpressed FtsI (PBP3) to target dividing chlamydial cells. The ORF
322 of chlamydial ftsI was cloned into our translational expression system and tagged with a C-terminal
323 3XFLAG epitope (13). The euoprom-mNG(LVA)_hctBprom-mKate2 promoter-reporter cassette was
324 cloned into the E-ftsI-3XFLAG vector and transformed into *Chlamydia* trachomatis L2 creating the strain
325 L2-E-ftsI-BMELVA. Ectopic expression of full length FtsI-FLAG in *Chlamydia* was verified by western
326 blotting (Fig. S2A). Ectopic FtsI expression resulted in a block in chlamydial replication as
327 demonstrated by inhibition of chromosome replication measured using digital droplet PCR (Fig. S2B).

Additionally, we examined the impact of FtsI overexpression on the RB population using immunofluorescence confocal imaging of host cells infected with L2-E-*ftsI*-BMELVA (Fig. S2C). Infected cells were treated with vehicle-only or induced for expression at 20 hpi. Inclusions from the 20 hpi and 30 hpi uninduced samples were filled with bacteria and contained multiple bright euoprom-mNG(LVA)+ cells, indicating the presence of live RBs capable of active transcription and translation (Fig. S2C). Conversely, inclusions from the 30 hpi FtsI induced samples were relatively empty compared to the 20 hpi and 30 hpi uninduced samples. A subset of cells in the induced sample stained positively for FLAG (i.e. indicating FtsI induction); these cells were misshapen and contained significantly less euoprom-mNG(LVA) fluorescence as compared to uninduced cells, indicating a lack of active expression and suggesting RB lysis had occurred (Fig. S2C).

An additional dual promoter reporter strain was created using *hctA*prom-mEos3.2 paired with *hctB*prom-mKate2 (L2-BMAMEO). The mEos3.2 GFP variant accumulates over time as it does not have the LVA degradation tag and will therefore be present in all cells that have expressed from the *hctA*prom (IBs and EBs). This dual color promoter reporter cassette was also cloned into the E-*ftsI*-3XFLAG plasmid and transformed into *Chlamydia*, creating L2-E-*ftsI*-BMAMEO. To differentiate between Asymmetric Production and Direct Conversion, cells were infected with L2-BMAMEO or L2-E-*ftsI*-BMAMEO and imaged from 10 hpi until 50 hpi (Fig. 6A, Experimental Data). Pen and Cip were added at 30 hpi to the L2-BMAMEO cultures and FtsI was induced by adding Theophylline (Tph) at 30 hpi to the L2-E-*ftsI*-BMAMEO infected cells to inhibit chlamydial replication. Live cell imaging of the *hctA*prom-mEos3.2 produced kinetics consistent with the Asymmetric Production model simulations. The increase of IB production signal from *hctA*prom was almost immediately inhibited by all three treatments (Fig. 6A, Experimental Data). As we have previously documented, the *hctA*prom reactivated in the Pen-treated aberrant cells after about an ~8 hour delay (11).

The two models also predicted differences in EB production when cell division was inhibited. The Asymmetric Production model predicted that EB production would halt ~6 hours after all treatments indicated (Fig. 6B, Asymmetric Production). The stochastic Direct Conversion model simulations predicted that inhibition of cell division would result in a slowing followed by a halt in EB production ~18 hour post treatment (Fig. 6B, Direct Conversion). To directly test these predictions, cells were infected with L2-BMAMEO or L2-E-*ftsI*-BMAMEO. Pen or Cip were added to L2-BMAMEO cultures and Tph was added to the L2-E-*ftsI*-BMAMEO infected cells at 30 hpi. EBs were collected every 4 hours from 10 to 50 hpi and used to infect fresh host cells for EB quantification. Our data show that EB production was inhibited ~8 hours post cell division inhibition with all three inhibitors (Fig. 6B, Experimental Data). These data taken together support a division dependent asymmetric IB production model and not stochastic direct conversion of an RB to an IB.

EB formation is independent of continued IB production. Both of our ABMs rely on the direct conversion of IBs into EBs without replication. To test this assumption, we infected cells with L2-BMELVA and used confocal imaging to assay for the expression of the EB associated promoter, *hctB*prom. Cells were infected with L2-BMELVA and replication was inhibited by treatment with Pen or Cip at 20 hpi. Untreated and treated samples were fixed and stained for DNA (DAPI) at 20 hpi and 30 hpi and imaged for DAPI, GFP and RFP fluorescence. Before treatment (20 hpi), all inclusions had *euo*prom+ cells (RBs), DAPI only positive cells (IBs), and no *hctB*prom+ cells (EBs) (Fig. 7A, S3A). At 30 hpi the untreated inclusions contained *euo*prom+ cells (RBs), DAPI only cells (IBs), and *hctB*prom+ cells (EBs) (Fig. 7B, S3A). The inclusions treated with Cip for 10 hours contained *euo*prom+ cells (RBs)

and *hct*Bprom+ cells (EBs) but less DAPI only cells (IBs) compared to untreated (Fig. 7B, S3B). Pen treated inclusions contained large aberrant *euo*prom+ cells (aberrant RBs), small *hctB*prom+ cells (EBs) and fewer DAPI only cells (IBs) at 30 hpi (Fig. 7B, S3C).

We also asked whether inhibiting cell division through FtsI ectopic expression affected IB to EB formation. Cells were infected with L2-E-*ftsI*-BMELVA and induced for FtsI expression at 20 hpi. The infected cells were fixed and stained with DAPI and confocal images were taken for DAPI, GFP, and RFP signals at 20 and 30 hpi. The inclusions in the L2-E-*ftsI*-BMELVA infected cells at 20 hpi contained *euo*prom+ cells (RBs) and DAPI only stained cells (IBs), and little to no *hctB*prom+ cells (EBs) (Fig. S3D, Fig. S4A). The uninduced L2-E-*ftsI*-BMELVA inclusions at 30 hpi contained *euo*prom+ cells (RBs), DAPI only positive cells (IBs), and a significant number of *hctB*prom+ cells (EBs) (Fig. S4B). However, the Tph induced L2-E-*ftsI*-BMELVA inclusions at 30 hpi had misshapen large chlamydial cells with just a trace of *euo*prom+ signal (RBs), fewer DAPI positive cells (IBs), and a significant number of *hctB*prom+ cells (EBs) (Fig. 7B, S3D). Taken together these data support the hypothesis that the IB matures directly into the EB cell form without undergoing cell division.

IBs convert directly to EBs. To verify that the IB directly matures into the EB without cell division (*hctA*prom+ to *hctA*prom+/*hctB*prom+), cells were infected with L2-BMAMEO to visualize the *hctA*prom+ and *hctB*prom+ cells, and cell division was inhibited with Cip at 18 hpi. Infected cells were then fixed and stained with DAPI at 22 hpi and 34 hpi. The inclusions were imaged for DNA (DAPI), GFP (*hctA*prom) and RFP (*hctB*prom) (Fig. 8A and B). The expression levels of GFP and RFP were determined for >500 individual chlamydial cells in three representative inclusions by identifying cells using the DAPI channel and measuring expression levels using the TrackMate plugin in FIJI (Fig. 8A and B). Confocal microscopy of untreated cells at 22 hpi revealed that there were a number of DAPI only (RBs) and *hctA*prom+ cells (IBs) with very few *hctA*prom+/*hctB*prom+ cells (IB->EBs) (Fig. 8A, UNT). At 34 hpi there were again populations of DAPI only (RBs) and *hctA*prom+ cells (IBs), however many of the *hctA*prom+ cells were also positive for *hctB*prom (IB->EB) (Fig. 8B, UNT). Similar trends were seen when cell division was inhibited by the addition of Cip at 18 hpi. The chlamydial population at 22 hpi consisted of primarily DAPI only (RBs) and *hctA*prom+ cell (IBs) (Fig. 8A, CIP), while many of the *hctA*prom+ cells were also *hctB*prom+ (IB->EB) by 34 hpi (Fig. 8B, CIP). This increase in the number of double positive cells in cell division inhibited *Chlamydia* suggests that the *hctA*prom+ cells were activating *hctB*prom over time.

We also asked whether the IB could directly become an EB after replication was inhibited by ectopic expression of FtsI. Cells were infected with L2-E-*ftsI*-BMAMEO and FtsI expression was induced at 18 hpi. At 22 hpi, there were a number of DAPI only (RBs) and *hctA*prom+ cells (IBs) in the induced population. Anti-FLAG staining revealed that many of the DAPI only cells were expressing FtsI-FLAG (Fig. 8A, FtsI). The inclusions at this time point contained very few *hctB*prom+ cells (EBs). At 34 hpi, there was a significant increase in the number of *hctA*prom/*hctB*prom double positive chlamydial cells (IB->EB), suggesting the *hctA*prom+ cells activated *hctB*prom without cell division (Fig. 8B, FtsI). The uninduced samples showed a similar pattern. These data together demonstrate that IBs (*hctA*prom+) mature directly into EBs (*hctB*prom+) and that cell division is not required for this progression.

Discussion

The developmental cycle of *Chlamydia* is central to its ability to cause disease. The cycle produces phenotypically distinct cell types with functional specificity. This includes the RB cell which replicates, leading to organism proliferation, and the EB cell type which mediates entry into new cells, disseminating the infection to new hosts. The developmental cycle has conventionally been broken down into two stages; RB replication and EB conversion. While the broad strokes of the overall cycle are described, the molecular details that regulate this process are poorly understood. Our data suggests that the current understanding of the cycle is an oversimplification. We propose that the developmental cycle can be divided into multiple stages including: EB germination, RB amplification/maturation, IB production, and EB formation.

Our data show that the chlamydial developmental cycle produces at least three different phenotypic cell types, the RB (*euo*prom+), IB (*hctA*prom+) and EB (*hctB*prom+). The data also demonstrate that RB proliferation initiates at ~10-12 hpi and reaches a plateau by 24-26 hpi after which RB numbers remain virtually unchanged until the end of the cycle. Remarkably, at the individual inclusion level the number of RBs at plateau was highly variable with some inclusions containing just a few RBs while others had as many as 60. To understand the potential mechanisms that underlie these observations, we developed computational agent based models (ABMs). Two mechanistic models were developed that could recapitulate our experimental data. Both models estimate the germination time based on published time to first RB replication (14) and time to *euo*prom expression (this study). The models differ primarily in the IB production mechanism which we hypothesize is the committed step to EB formation. Regulatory mechanisms such as RB access to or competition for inclusion membrane contact (19), reduction in RB size (8), and responses to changes in nutrient availability (20), have been proposed to explain the regulation of EB formation. Although the triggering signal for differentiation differs in these models, all propose a stochastic direct RB to EB conversion mechanism. Therefore, the Direct Conversion Model utilized a direct conversion mechanism to control RB amplification and IB production. Our second ABM, the Asymmetric Production Model, used a RB maturation/asymmetric division mechanism to control RB amplification and IB production. In this model, we proposed two RB subtypes; the RB_R which upon replication produces two identical RB_R daughter cells, and a RB_E that upon cell division produces one IB and one RB_E. The RB_R subtype matures into the RB_E subtype during the first 24 hours of infection. For both models, the IB cell exits the cell cycle and matures directly into the EB. Although both models could reproduce the measured kinetics of the developmental cycle at the population level, only the maturation/asymmetric model could reliably reproduce the observed kinetics at the single inclusion level. Even after constraining replication and conversion to avoid RB extinction or overpopulation, the stochastic direct conversion model resulted in runs of over and under IB production that were not readily evident in the measured data.

The Asymmetric Production model predicted that the mature RB cell (RB_E) acts as a stem cell, producing one IB upon division while the other daughter cell remains an RB_E. The Direct Conversion model predicted that RB numbers are at steady state where cell division creates new RBs while other RBs convert into IBs. Using live cell microscopy, we determined that individual RBs were consistently present and trackable from time point to time point over a 30 hour time period, strongly suggesting the RB population is acting like stem cells and not a steady state population. Conversely, both models predicted that the IB population is at steady state, with IBs forming and transitioning into EBs while new IBs replace those that became EBs. The behavior of individual IBs revealed by live cell imaging was consistent with a steady state population, with IBs disappearing and new ones appearing over time.

The models also predicted that inhibition of cell replication would have differing effects on the RB, IB and EB populations. The stochastic Direct Conversion model predicted that RB numbers would decline after cell division inhibition as RBs that directly converted to IBs were not replaced by new RBs through cell division. In contrast, the Asymmetric Production model predicted that inhibition of cell division would have no impact on the RB population. We found that treatment with two different cell replication inhibitors (Pen and Cip) resulted in no decrease in the RB population over a 10 hour period, again strongly supporting an asymmetric division model.

The kinetics of the IB and EB population was also predicted to differ in the two models after replication was inhibited. The Direct Conversion model predicted that inhibition of cell division would lead to a protracted inhibition of new IB formation, resulting in decreasing IB production over ~12 hours, while EB formation would also slowly decline until completely inhibited at ~18 hours after treatment. The Asymmetric Production model predicted that inhibiting cell division would inhibit new IB production nearly immediately and inhibit EB formation after the ~8 hour IB to EB maturation time (11). Live cell microscopy demonstrated that the kinetics of cell division inhibited *Chlamydia* which clearly supported the Asymmetric Production model over the Direct Conversion model as IB production halted nearly instantly and EB production halted after ~8 hours.

Both models predicted that IBs mature directly into EBs. This prediction is supported by the data showing that the IB cell type progressed to *hctB*prom expression after inhibiting cell division with Cip, Pen or through ectopic expression of FtsI. Additionally, we demonstrated that IBs mature directly from *hctA*prom single positive to *hctA*prom/*hctB*prom double positive cells even after inhibiting cell division with Cip or overexpression of FtsI.

Cell size has been proposed as a mechanism controlling stochastic RB to IB conversion. The average chlamydial cell size becomes smaller and more heterogeneous over time (8). Our asymmetric production model also predicts that cell size will behave similarly, decreasing in size and increasing in heterogeneity over time. In our model, early in the developmental cycle the RBR cell progresses through the cell cycle and divides to produce two RBRs which immediately re-enter the cell cycle gaining mass before the next division. As the cycle progresses RBRs mature into RBEs. The RBE continues in the cell cycle and upon division produces one RBE and one IB. After division the RBE remains in the cell cycle increasing in size, however the IB does not re-enter the cell cycle and does not begin to add mass and is therefore smaller than the RBR/E cells. The IB then proceeds to reduce in volume as it matures to the EB cell over a ~8 hour time frame (11). This process would produce IB cells of varying sizes with a trend towards smaller and smaller cells in the inclusion as early IBs increase in number compared to RBs.

Overall, the data support a developmental cycle that includes an asymmetrically dividing RB population. Asymmetry has been documented for both the EB and RB cell (21–24). In addition, it has been shown that the division plane can form asymmetrically during RB division (21, 25). Asymmetric cell division is a common mechanism to generate phenotypically distinct cell populations in bacteria. Many of these systems have evolved to create two cell populations; one cell acts as the stem cell while the other cell disseminates the bacterial colony to new environments. Both *Caulobacter crescentus* and some members of *Chlamydia's* nearest phylogenetic neighbors, the *Planctomycetes,* undergo a division cycle that includes a surface attached mother cell that produces a planktonic swarmer cell upon division in order to extend the population to new ecological niches (26, 27). The swarmer cell in the case of *C. crescentus* is non replicating and is out of the cell cycle (28). Our data support a similar role for the EB cell as the EB disseminates the infection, does not replicate, and is out of the cell cycle (17).

The mother/swarmer cell developmental model fits our data for IB/EB production, but does not explain RB expansion. We have modeled this process (RB expansion to RB/IB asymmetric division) as maturation over time from an RB that produces two RBs thereby increasing the dividing cell population (RB_R), to a RB mother/stem cell (RB_E) that produces an IB through asymmetric division. Currently the mechanism for RB_R to RB_E maturation is unknown but could be influenced by several factors such as EB age at infection, differences in nutrient acquisition, the effects of inclusion membrane interaction or through a yet to be described stochastic maturation mechanism. Additionally, our data show that this expansion step produces significant heterogeneity in RB_E numbers in individual inclusions. This differential amplification is potentially a novel evolutionary adaptation to balance RB maturation and early EB production, i.e late maturation leads to late EB production but a high EB production rate, whereas early maturation leads to early EB production with a low EB production rate. We currently have no expression markers that show differences between the two theoretical RB sub types, the RBR and the RBE. Our data and subsequent model suggest that this is the best explanation for our data and will be a continuing area of investigation.

The Asymmetric Model suggests that asymmetry is generated during cell division after a maturation process. We have not, however, detected differential expression between forming daughter cells during division using our currently available dual color promoter reporters. The two forming daughter cells appear to express similar levels of fluorescence from the *euo*prom-mNG(LVA) reporter and also appear to be similar sizes. This has been reported by other studies that showed that although there is evidence that the division plane initiates asymmetrically, at cytokinesis the two daughter cells appear to be of similar size (8,18,24,25). Our data suggests that differential gene regulation of the *hctA* promoter in the two daughter cells happens after the cells have separated thereby increasing the difficulty in identifying the daughter cell pairs.

Our data support a four-stage model, EB germination, RB amplification/maturation, IB production, and EB formation (Fig. 9). A key aspect of this model is the stochastic amplification and maturation of RBs (RB_R) from an expanding population to a stem cell RB population (RB_E) that produces IBs through asymmetric replication reminiscent of stalk/swarmer cell dynamics (Fig. 9). This is followed by an EB formation stage where the IB undergoes a dramatic phenotypic change that includes the expression of the nucleoid associated protein HctA and ultimately ends with the expression of a second nucleoid associated protein HctB. This EB formation stage takes ~8-10 hours, ultimately resulting in the infectious EB (11) (Fig. 9). Our model suggests that the cycle starts with RB amplification and quickly converts to a mixed environment of RB_Rs producing RBs, and RB_Es producing IBs. The IB phenotype takes ~8-10 hours to complete maturation into the infectious EB. Our data suggest that replication is significantly faster than IB to EB maturation therefore IBs accumulate and are a significant cell type in the inclusion for most of the cycle, outnumbering RBs as soon as ~18 hpi. It is currently unclear what role the IB cell type has in the cell biology of the chlamydial infection.

Temporal gene expression during the chlamydial infection has been extensively reported at the population level. These data have historically categorized developmental gene expression into early, mid and late expressed genes (7,29). However, these studies were all performed at a population level and normalized accordingly. Our model and supporting data suggest that this gene expression cascade is explained by a shift in cell types within the inclusion. Early in the cycle (~10-16 hpi) the inclusion is dominated by RB cells, by 18 hpi there is a mix of RBs and IBs and by 24hpi early IBs have matured into EBs and IBs begin to outnumber the RBs. Additionally, from 30 hpi and on EBs quickly accumulate

546 becoming the dominant cell form overwhelming the gene expression signal of the other cell types. Our
547 data suggest that to fully understand the developmental cycle, the kinetically dynamic mixed cell
548 environment needs to be taken into consideration.
549 Our experiments and models have focused on *Chlamydia serovar L2* living in close to ideal
550 growth conditions (11) However, the developmental cycle is shared by all of the Chlamydiaceae family.
551 Our studies focused on serovar L2 as it has become established as a model organism for
552 understanding the basic life cycle of these organisms as it lends itself to genetic manipulation and
553 infects cultured cells efficiently. Our studies are likely to result in a further understanding of the
554 chlamydial developmental cycle across the family. Eventually we would like to determine if what is
555 reported here describes all the *Chlamydia* species and chlamydial-like organisms but further studies
556 are needed. Additionally, it is likely that *Chlamydia* reacts and adapts the cycle to nutrient and other
557 stresses. The creation of an ABM that models the mechanisms of the developmental cycle under ideal
558 conditions will provide a tool to visualize and understand the convolved data obtained from nutrient
559 limiting, pharmacological, genetic, and molecular experiments. Ultimately, a better mechanistic
560 understanding of the developmental cycle will lead to novel therapeutics targeting development as
561 breaking the cycle will eliminate dissemination and chlamydial disease.
562
563 **Materials and Methods**
564 **Organisms and cell culture.** Cos-7 cells were obtained from (ATCC). Cells were maintained in a
565 5% CO2 incubator at 37°C in RPMI 1640 (Cellgro) supplemented with 10% fetal plex (FP) and 10mg/ml
566 gentamicin. All *C. trachomatis* L2-bu434 (L2) strains were harvested from Cos-7 cells. Elementary
567 bodies were purified by density centrifugation using 30% MD-76R at 48 hours post infection(29).
568 Purified elementary bodies were stored at -80°C in sucrose-phosphate-glutamate buffer (SPG) (10 mM
569 sodium phosphate [8 mM K 2HPO 4, 2 mM KH 2PO 4], 220 mM sucrose, 0.50 mM L-glutamic acid; pH
570 7.4). *Escherichia coli* ER2925 (*dam⁻/dcm⁻*) was utilized to produce unmethylated plasmids for
571 transformation into *Chlamydia*.
572 **Promoter reporter and inducible expression constructs.** All constructs were created in the
573 p2TK2SW2 plasmid background (30). Promoters and the *ftsI* ORF were amplified from *C. trachomatis*-
574 L2 (LGV Bu434) genomic DNA using the indicated primer**s (**Table S1**).** Fluorescent reporters were
575 ordered as gBlocks and cloned using the In-fusion HD EcoDry Cloning kit (Takara). Promoter reporter
576 constructs were created as previously described (11, 31). The p2TK2SW2-E-*ftsI*3XFLAG was
577 generated by replacing the *clover* gene with the *ftsI* ORF in the previously created p2TK2SW2-E-
578 clover-3XFLAG plasmid (32). Dual promoter reporter cassettes (*euo*prom-mNG(LVA)_*hctB*prom-
579 mKate2 and *hctA*prom-mEos3.2_*hctB*prom-mKate2) were then inserted upstream of E-*ftsI*-3XFLAG to
580 produce the p2TK2SW2-E-*ftsI*-3XFLAG_*euo*prom-mNG(LVA)_*hctB*prom-mKate2 and p2TK2SW2-E-
581 *ftsI*-3XFLAG_*hctA*prom-mEos3.2_*hctB*prom-mKate2 constructs.
582 **Chlamydial transformation and isolation.** Transformation of *C. trachomatis*-L2 was performed as
583 previously described with selection using 500 ng/ul spectinomycin (30). Clonal isolation of
584 transformants was achieved by inclusion isolation (MOI <1) via micro-manipulation. To confirm clonality
585 each construct was purified from the chlamydial transformants, transformed into *E. coli* and five
586 colonies were sequenced. The resulting strains are summarized in Table 1.
587 **Infections.** Infections were synchronized by incubating Cos-7 cells with *C. trachomatis*-L2 EBs in
588 Hank's balanced salt solution (HBSS) (Gibco) for 15 minutes at 37ºC while rocking. The inoculum was
589 removed and cells were washed with prewarmed (37ºC) HBSS with 1 mg/ml heparin. The HBSS was

590 replaced with fresh RPMI-1640 containing 10% FP, 10 µg/ml gentamicin, 1 µg/ml cycloheximide, and 1
591 mg/ml heparin sodium. Chlamydial cell division was inhibited by the addition of 0.5 µg/ml ciprofloxacin
592 or 1 U/ml penicillin-G to the media. Expression of *ftsI*-3XFLAG was induced by the addition of 0.5 mM
593 theophylline to the media (32).
594 **Replating assays.** EBs were isolated from infected Cos-7 cells by scraping the host monolayer
595 followed by centrifugation at 4ºC for 30 min at 18213 rcfs. EB pellets were resuspended in 4ºC RPMI
596 via sonication and used to infect Cos-7 cells in polystyrene 96-well microplates in a 2-fold dilution
597 series. Infected cells were incubated for 29 hours followed by methanol fixation. Fixed cells were
598 stained with 4′,6-diamidino-2-phenylindole (DAPI) for visualization of host-cell nuclei and anti-MOMP
599 antibody conjugated to FITC (Thermo Scientific™) for visualization of *Chlamydia*. Monolayers were
600 imaged with an Andor Zyla sCMOS and Nikon Eclipse TE300 inverted microscope and the scopeLED
601 illumination system at 470nm and 390nm, and BrightLine band pass emissions filters at 514/30nm and
602 434/17nm. Automated image acquisition was performed using µManager software (33). Inclusion
603 numbers were quantified with custom scripts in ImageJ and analyzed in custom Python notebooks as
604 previously described (11, 29, 31)
605 **Genome number quantification.** Total DNA was isolated from infected Cos-7 cells during active
606 infections using an Invitrogen Purelink genomic DNA mini kit. A QX200 digital droplet system (BioRad)
607 was utilized for quantification of chlamydial genomic copies. A 2X ddPCR™ Supermix for Probes-No
608 dUTP kit (BioRad) and a custom *copN*-specific primer/probe set was used for DNA detectio**n (**Table
609 S1**).**
610 **Live-cell microscopy.** Monolayers were seeded on a multi-well glass-bottom plate and infected
611 with *Ctr*-L2 EBs. Infections were grown in an OKOtouch CO2/heated stage incubator. Fluorescence
612 images were acquired via epifluorescent microscopy using a Nikon Eclipse TE300 inverted microscope
613 with a ScopeLED lamp at 470nm and 595nm, and BrightLine Bandpass filters at 514/30nm and
614 590/20nm. 20X/0.4NA dry, 40X/0.6NA dry, and 60X/1.40NA oil objective lenses were used. DIC was
615 used to auto-focus images. Image acquisition was performed using an Andor Zyla sCMOS camera in
616 conjugation with µManager software (33). Images were taken in 30 min intervals, unless otherwise
617 stated. Imaging ranged from 10 to 60 hours after *Ctr*-L2 infection, depending on the experiment.
618 Multiple fields were imaged for each treatment and the fluorescent intensity of individual inclusions was
619 monitored using the TrackMate plug-in in FIJI (12). Inclusion fluorescent intensities were averaged and
620 graphed in Python as previously described (31)
621 **Confocal microscopy.** Cos-7 cells were seeded onto glass coverslips and infected with the
622 appropriate *Ctr*-L2 strains. Samples were fixed at the designated times in 2% paraformaldehyde in
623 phosphate-buffered saline (PBS) at room temperature, overnight. Samples were then washed with
624 filtered PBS and stained with DAPI to visualize DNA and monoclonal anti-FLAG M2 antibody (Sigma,
625 Thermo Scientific™) with alexa 647 anti-mouse secondary antibody to visualize FtsI-3XFLAG
626 expression. Coverslips were mounted onto a microscope slide using MOWIOL (100 mg/mL 150
627 MOWIOL® 4-88, 25% glycerol, 0.1 M Tris pH 8.5). Images were acquired using a Nikon spinning disk
628 confocal inverted microscope with a 100X/1.45NA oil objective with a laser lamp at 405nm, 490nm,
629 568nm and 660nm. Image acquisition was performed using an Andor Ixon EMCCD camera and the
630 Nikon elements software. Collected images were taken as z stacks at 0.2 µm intervals capturing the
631 entirety of each inclusion. Multiple inclusions were imaged for each treatment/time point and
632 quantification of individual cells was performed using TrackMate. Chlamydial cell numbers were then

analyzed in custom Python notebooks. Representative confocal micrographs are maximal intensity projections of 3D data sets and brightness and contrast was adjusted equally for comparisons.

Western Analysis. To ensure that ectopically expressed FtsI was full size, Infected monolayers were lysed in reducing lane marker sample buffer and protein lysates were separated on a 6% SDS-PAGE gels and transferred to a Nitrocellulose Membrane for western analysis of the FLAG-tagged protein. The membrane was blocked with PBS + 0.1% Tween 20 (PBS-T) and 5% nonfat milk prior to incubating in monoclonal anti-FLAG M2 antibody (1:40,000, Sigma, Thermo Scientific™). overnight at 4 ºC followed by Goat-anti Mouse IgG-HRP secondary antibody (Invitrogen™) at room temperature for 2 hours. The membrane was developed with the Supersignal West Dura luminol and peroxide solution (Thermo Scientific™) and imaged using an Amersham Imager 600.

Computational Modeling. Modeling was done using the CellModeller platform (13). The model description scripts, and model data analysis scripts are described in supplemental information and available on github (SGrasshopper/Chlamydial-developmental-cycle).

Data Availability. All data, bacterial strains and methodologies are available upon request.

Funding: This work was supported by National Institutes of Health Grants R01AI130072, R21AI135691 and R21AI113617 (NG, SG). Additional support was provided by the Institute for Modeling Collaboration and Innovation (IMCI) Data Access Grant from the University of Idaho and pilot Grant (NIH COBRE P20GM104420).

Figure Legends:

Figure 1: Dual cell-form specific promoter reporter chlamydial strains reveal three distinct chlamydial cell populations. A. Representative single z-plane confocal micrographs of Cos-7 cells infected with C*tr*-L2-*hctB*prom-mKate2_*euo*prom-Clover (L2-BMEC), *Ctr*-L2-*hctB*prom-mKate2_*euo*prom-mNG(LVA) (L2-BMELVA), *Ctr*-L2-*hctA*prom-mKate2_*euo*prom-mNG(LVA) (L2-AMELVA) and *Ctr*-L2-*hctB*prom-mKate2_*hctA*prom-mNG(LVA) (L2-BMALVA) reporter strains. The infections were fixed at 24hpi and imaged. For L2-BMEC, Clover (green), mKate2 (red) and DAPI (cyan) images are shown. For L2-BMELVA, L2-AMELVA, and L2-AMALVA, mNG(LVA) (green), mKate2 (red) and DAPI (cyan) images are shown. Magnified FOVs for L2-BMELVA, L2-AMELVA, and L2-BMALVA demonstrate cell-form specific expression in individual cells. While the L2-BMEC expressing chlamydial cells show green only cells and red and weakly green cells. Scale bar = 10 µm. Quantification of both the GFP and RFP channels of GFP (Clover or mNG(LVA) and mKate2 positive cells was performed using TrackMate from 4 individual inclusions per strain. The red dots each represent a single RFP expressing cell while the green dots represent GFP expressing cells. The measured fluorescent values from each channel for both cell types were plotted (Y axis = RFP and X axis = GFP fluorescent signal). Chlamydial cells from L2-BMEMC infections demonstrate overlapping GFP and RFP expression in RFP positive cells, while RFP and GFP expressing cells are distinct populations for L2-BMELVA, L2-AMELVA and L2-BMALVA. **B.** Live-cell expression kinetics of L2-BMELVA, L2-AMELVA and L2-BMALVA reporter strains from n>20 individual inclusions. Infections were imaged from 10-50 hpi via automated live-cell fluorescence microscopy. Average intensities are shown, cloud represents SEM.

677
678 **Figure 2: IB and EB production is dependent on the number of RBs.** Cos-7 cells were infected with
679 purified *Ctr*-L2-prom EBs. **A.** Live-cell expression kinetics from single inclusions from L2-AMELVA
680 infected cells. Graphs show *euo*prom-mNG(LVA) expression, *hctA*prom-mKate2 expression, and
681 *hctA*prom-mKate2 expression normalized to the paired average expression levels of *euo*prom-
682 mNG(LVA) between 30-38 hpi. **B.** Live-cell expression kinetics from single inclusions of L2-BMELVA
683 infected cells. Graphs show *euo*prom-mNG(LVA) expression, *hctB*prom-mKate2 expression, and
684 *hctB*prom-mKate2 expression normalized to the paired average expression levels of *euo*prom-
685 mNG(LVA) between 30-38 hpi. n>20 inclusions per treatment. **C and D.** Quantification of *euo*prom+ or
686 *hctA*prom+ cell counts within individual inclusions from fixed samples. Infections were fixed every two
687 hours from 14-48 hpi and stained with DAPI. Inclusions were imaged by confocal microscopy for DAPI,
688 GFP and RFP. Individual dots represent the number of promoter reporter+ chlamydial cells within
689 individual inclusions. Solid line represents the mean number of promoter reporter+ cells per time point.
690 Sample size ranged between 3-14 inclusions dependent on the time point. Cloud represents 95% ci.
691
692 **Figure 3: Simulations of inclusion kinetics from the Asymmetric Production and Direct**
693 **Conversion models. A.** Simulated developmental kinetics of the Asymmetric Production and Direct
694 Conversion models. RBs: green, IBs: blue, and EBs: pink. **B.** Simulated kinetics of the Direct
695 Conversion model if conversion outcompetes replication (Panel 1) or replication outcompetes
696 conversion (Panel 2). **C.** Individual traces of simulated RB and EB kinetics on a per-inclusion level for
697 the Asymmetric Production and Direct Conversion models. Colors of individual inclusion traces are
698 paired between the RB and EB cell forms per model simulation. Infections were simulated from 0-50
699 hpi. For **A and B,** the average of 20 simulations/model are shown, cloud represents SEM. Model
700 parameters can be found in **Supplemental Materials**.
701
702 **Figure 4: RBs persist as a stem cell population while IBs are at steady state.** Cos-7 cells were
703 infected with either (**A**) L2-BMELVA (RB/EB) or (**B**) L2-BMALVA (IB/EB). Individual inclusions were
704 imaged using a 40X objective every 15 min from 24-60 hpi. Numbered arrowheads indicate individual
705 *euo*prom-mNG(LVA)+ (RB) or *hctA*prom-mNG(LVA)+ (IB) cells through time. (**A**) Two binary division
706 events occurred between 26 to 31 hpi, corresponding to cells 3a/b and 5a/b. Scale bar = 10 µm. The 15
707 min interval time lapse videos for each inclusion can be found in supplemental material (**Mov. S3** and
708 **S4)**.
709
710 **Figure 5: RBs do not convert into IBs after cell division inhibition.** Simulated cell-form kinetic of
711 cell division inhibition in the Asymmetric Production (**A**) and Direct Conversion model (**B**). RBs: green,
712 IBs: blue, and EBs: pink. Infections were simulated from 0-50 hpi. Gray vertical line indicates time of
713 simulated cell-division inhibition (30 hpi). Average cell form subpopulation numbers of 20 simulations
714 per model are shown, cloud represents SEM. **C.** Cos-7 cells were infected with purified L2-BMELVA
715 EBs. Infected cells were treated at 30 hpi with either vehicle (UNT), penicillin-G (PEN) or ciprofloxacin
716 (CIP). The number of *euo*prom-mNG(LVA)+ cells were counted per inclusion at 30 and 40 hpi.
717 Horizontal lines connect the same imaged inclusions. **D.** Boxplot demonstrating the 40/30 hpi ratio of
718 RBs per treatment. The center gray line represents the median number of RBs, the yellow triangle
719 represents the mean.
720

721 **Figure 6: IB and EB production halt after cell division inhibition. A.** Simulated kinetic outputs of the
722 total accumulation of GFP from the IB-associated promoter *hctA*prom for both the Asymmetric
723 Production and Direct Conversion models. **B.** Simulated total EB cell numbers for both the Asymmetric
724 Production and Direct Conversion models. Untreated: green, cell-division inhibition: blue. Infections
725 were simulated from 0-50 hpi. Average of 20 simulations per model are shown. **A and B, Experimental**
726 **data.** Cos-7 cells were infected with L2-*ftsI*-3XFLAG-BMAMEO (FtsI induction) or L2-BMAMEO (PEN
727 and CIP). Infected cells were treated at 30 hpi with vehicle (UNT): green, penicillin-G (PEN): purple,
728 ciprofloxacin (CIP): blue, or induced for FtsI: orange. **A, Experimental Data.** Mean expression kinetics
729 of *hctA*prom-mEos3.2. **B, Experimental data.** Mean number of infectious progeny. Arrow indicates
730 time of treatment (30 hpi). Horizontal solid line indicates the time to inhibition of IB or EB formation.
731 Cloud for simulations and fluorescent reporters represents SEM. n>20 inclusions per treatment. IFU
732 cloud represents 95% ci.
733
734 **Figure 7: IB to EB development is replication independent.** Cos-7 cells were infected with either
735 purified L2-BMELVA or L2-E-*ftsI*-3XFLAG-BMELVA. L2-BMELVA infected cells were treated with either
736 vehicle (UNT), ciprofloxacin (CIP), or penicillin-G (PEN) and L2-E-*ftsI*-3XFLAG-BMELVA infected cells
737 were induced for FtsI at 20 hpi. Samples were fixed at 20 hpi (pre-treatment) or 30 hpi, and stained with
738 DAPI. Images are z projected confocal micrographs showing *euo*prom-mNG(LVA): green, *hctB*prom-
739 mKate2: red, and DAPI: cyan. **A.** Representative confocal micrograph of a 20 hpi inclusion. **B.**
740 Representative confocal micrographs of 30 hpi UNT, CIP, PEN and FtsI-induced infections. Insert
741 demonstrates positive anti-FLAG staining in the FtsI-induced sample. Scale bar = 10 µm. See
742 supplemental Fig. S3 for chlamydial cell quantification and Fig. S4 for the uninduced FtsI sample.
743
744 **Figure 8: IBs mature directly into EBs.** Cos-7 cells were infected with L2-E-*ftsI*-3XFLAG-BMAMEO.
745 Infected cells were treated at 18 hpi with either vehicle (UNT), ciprofloxacin (CIP), or induced for FtsI-
746 3XFLAG expression (FtsI). Samples were fixed at 22 hpi or 34 hpi, stained with DAPI and an anti-FLAG
747 antibody. Images are z-projections from confocal micrographs showing *hctA*prom-mEos3.2: green,
748 *hctB*prom-mKate2: red, DAPI: cyan, anti-FLAG: magenta. **A.** Representative confocal micrographs of
749 22 hpi cells along with quantification of *hctA*prom-mEos3.2 and *hctB*prom-mKate2 expression levels at
750 the single cell level. Quantification of DAPI positive cells was performed using TrackMate from 3
751 individual inclusions per treatment per time point. Each color corresponds to chlamydial cells quantified
752 within the same inclusion. **B.** Confocal micrographs of L2-E-*ftsI*-3XFLAG-BMAMEO infected cells at 34
753 hpi either treated with vehicle (UNT), CIP, or induced to express FtsI. Inserts demonstrate the overlap
754 of *hctA*prom-mEos3.2 and *hctB*prom-mKate2 within single cells. Quantification of DAPI positive cells
755 was performed using TrackMate from 3 individual inclusions per treatment per time point. Each color
756 corresponds to chlamydial cells quantified within the same inclusion. n = > 500 cells per treatment.
757 Scale bar = 10 µm.
758
759 **Figure. 9. Model of the developmental cycle. A.** Cell-form specific live-cell kinetics from Figure 1. **B.**
760 Simulated developmental cycle using the asymmetric division/maturation model. **C.** Schematic of the
761 developmental model. Model consists of: EB to RB germination, RB amplification/maturation,
762 asymmetric IB production, and direct IB to EB formation. RBs (*euo*): green; IB (*hctA*): blue>black>red;
763 EB (*hctB*): pink.
764

765 Table 1. List of reporter strains and their relevant promoter constructs.
766
767 **Supplemental figures**
768
769 **Figure S1: Schematic representation of the dual promoter reporter constructs.** Promoter reporter
770 cassettes were cloned into p2TK2SW2. Cassettes were inserted between the orfs of *pgp7* and *pgp8*. **A.**
771 p2TK2SW2-AMELVA encodes *hctA*prom-mKate2 and *euo*prom-mNeonGreen(LVA), **B.** p2TK2SW2-
772 BMELVA: *hctA*prom-mKate2 and *euo*prom-mNeonGreen(LVA) and **C.** p2TK2SW2-BMALVA:
773 *hctB*prom-mKate2 and *hctA*prom-mNeonGreen(LVA).
774
775 **Figure S2: DNA replication is inhibited by ciprofloxacin treatment and FtsI overexpression. (A).**
776 **Western blot of FtsI-3xFLAG**. Cos-7 cells were infected with E-*ftsI*-3xFLAG-BMELVA. FtsI expression
777 was induced by adding media with 0.5 mM theophylline at 20 hpi and harvest at 22hpi. Uninduced
778 biological replicates (UNT) showed no protein expression. Induced samples (IND) revealed protein
779 bands at 70kd, the expected size of the FtsI-3xFLAG protein. **(B).** Cos-7 cells were infected with L2-
780 BMELVA EBs. Infected cells were treated at 30 hpi with vehicle-only (UNT): green, penicillin-G (PEN):
781 purple, or ciprofloxacin (CIP): blue. Additionally, Cos-7 cells were infected with L2-E-*ftsI*-3XFLAG-
782 BMELVA and induced for FtsI-3XFLAG expression at 30 hpi with 0.5 mM theophylline (FtsI) or vehicle-
783 only (UNT). Samples were harvested every 4 hours from 26-54 hpi. Genome copies were quantified
784 using ddPCR. Arrow indicates treatment time. Means are shown. Cloud represents 95% ci. **(C**).
785 Representative fixed confocal z-projection micrographs of Cos-7 cells infected with L2-*ftsI*-3XFLAG-
786 BMELVA at 20 hpi and after induction for FtsI-3XFLAG expression with 0.5 mM theophylline or vehicle-
787 only for 10 hours (30 hpi). Fixed samples were stained with DAPI and anti-FLAG. Arrowheads and
788 insert demonstrates FLAG expression and weak *euo*prom expression in misshapen chlamydial cells.
789 Scale bar = 10 µm.
790
791 **Figure S3: Single-cell quantification of EB production with cell replication inhibitors.** Cos-7 cells
792 were infected with L2-BMELVA (**A-C**) or L2-*ftsI*-3XFLAG-BMELVA (**D**). Infected cells were treated with
793 **A**: UNT, **B**: CIP, **C**: PEN, or **D**: induced for FtsI at 20 hpi. Cells were fixed and stained for DAPI at 20
794 and 30 hpi and imaged using confocal microscopy. Expression of DAPI and *hctB*prom-mKate2 was
795 quantified on a single-cell basis using TrackMate from 3 individual inclusions per treatment per time
796 point. Each color corresponds to chlamydial cells quantified within the same inclusion. n>500
797 cells/treatment.
798
799 **Figure S4: Confocal micrograph of uninduced L2-*ftsI*-3XFLAG-BMELVA.** Representative fixed z
800 projected confocal micrographs of Cos-7 cells infected with L2-*ftsI*-3XFLAG-BMELVA at 20 hpi (**A**) and
801 30 hpi (**B**). Fixed samples were stained with DAPI and anti-FLAG. Insert demonstrates the lack of
802 FLAG expression in both samples. Scale bar = 10 µm.
803
804 **Movie S1: Single inclusion simulation of the Asymmetric Production model.** Simulated individual
805 cell-form development of a single inclusion. Germinating EB: lavender, RBs: green, IBs:
806 blue>black>red, and EBs: pink. The green circle follows the progression of three RBs. Individual RBs
807 persist throughout the cycle demonstrating stem cell-like properties.
808
809 **Movie S2: Single inclusion simulation of the Direct Conversion model.** Simulated individual cell-
810 form development of a single inclusion. Germinating EB: lavender, RBs: green, IBs: blue>black>red,

811 and EBs: pink. The green circle follows the progression of multiple individual RBs. Individual RBs are
812 transient as they convert into IBs. However, RB division is matched with RB-to-IB conversion, leading
813 to a fluctuating steady-state in RB numbers.
814
815 **Movie S3: Live-cell time-lapse movie of RB stability throughout an active infection.** Cos-7 cells
816 were infected with L2-BMELVA. 40X automated live-cell fluorescence microscopy was used to monitor
817 individual RBs (*euo*prom-mNG(LVA)+ cells) within single inclusions every 15 minutes from 24-60 hpi.
818 The *hctB*prom-mKate2 promoter reporter was used for inclusion identification and to monitor chlamydial
819 development.
820
821 **Movie S4: Live-cell time-lapse movie of transient IBs throughout an active infection.** Cos-7 cells
822 were infected with L2-BMALVA. Automated live-cell fluorescence microscopy was used to monitor
823 individual IBs (*hctA*prom-mNG(LVA)+ cells) within single inclusions every 15 minutes from 24-60 hpi.
824 The *hctB*prom-mKate2 promoter reporter was used for inclusion identification and to monitor chlamydial
825 development.
826
827 **SM1 Model description:** Description of Agent-based Models.
828
829 **Table S1.** List of primers used in the construction of the plasmids and ddPCR experiments used in this
830 study.
831
832 **References:**

833 1. Mumtaz G, Sharara E, Dejong J, Sibai A, Roberts B, Abu-Raddad L. 2019. P800Prevalence of
834 curable sexually transmitted infections among refugees: global systematic review and meta-
835 analysis.
836 2. States C on P and C of STI in the U, Practice B on PH and PH, Division H and M, Medicine NA of
837 S Engineering, and, Vermund SH, Geller AB, Crowley JS. 2021. Sexually Transmitted Infections:
838 Adopting a Sexual Health Paradigm. Retrieved 26 July 2021.
839 3. Abdelrahman YM, Belland RJ. The chlamydial developmental cycle. FEMS microbiology reviews
840 29:949959.
841 4. Clifton DR, Fields KA, Grieshaber SS, Dooley CA, Fischer ER, Mead DJ, Carabeo RA, Hackstadt
842 T. A chlamydial type III translocated protein is tyrosine-phosphorylated at the site of entry and
843 associated with recruitment of actin. Proceedings of the National Academy of Sciences of the
844 United States of America 101:1016610171.

845 5. Hackstadt T, Baehr W, Ying Y. 1987. Chlamydia trachomatis developmentally regulated protein is
846 homologous to eukaryotic histone H1. Proceedings of the National Academy of Sciences of the
847 United States of America 88:39373941.
848 6. Kaul R. 1995. Eukaryotic-like histones in Chlamydia. Frontiers in Bioscience.
849 7. Belland RJ, Zhong G, Crane DD, Hogan D, Sturdevant D, Sharma J, Beatty WL, Caldwell HD.
850 Genomic transcriptional profiling of the developmental cycle of Chlamydia trachomatis.
851 Proceedings of the National Academy of Sciences of the United States of America 100:84788483.
852 8. Lee JK, Enciso GA, Boassa D, Chander CN, Lou TH, Pairawan SS, Guo MC, Wan FYM, Ellisman
853 MH, Stterlin C, Tan M. 2016. Replication-dependent size reduction precedes differentiation in
854 Chlamydia trachomatis. Nature Communications 9:45.
855 9. Rockey DD, Matsumoto A. 2000. The chalmydial developmental cycle. Prokaryotic Development.
856 ASM Press, Washington D. C.
857 10. Abdelrahman YM, Belland RJ. 2005. The chlamydial developmental cycle. FEMS Microbiology
858 Reviews. Oxford University Press.
859 11. Chiarelli TJ, Grieshaber NA, Omsland A, Remien CH, Grieshaber SS. 2020. Single-Inclusion
860 Kinetics of Chlamydia trachomatis Development. MSystems. American Society for Microbiology.
861 12. Tinevez J-Y, Perry N, Schindelin J, Hoopes GM, Reynolds GD, Laplantine E, Bednarek SY, Shorte
862 SL, Eliceiri KW. 2015. TrackMate: An open and extensible platform for single-particle tracking.
863 Methods 115:8090.
864 13. Rudge TJ, Steiner PJ, Phillips A, Haseloff J. 2012. Computational modeling of synthetic microbial
865 biofilms. ACS Synthetic Biology. American Chemical Society (ACS).
866 14. Miyairi I, Mahdi OS, Ouellette SP, Belland RJ, Byrne GI. 2006. Different growth rates of Chlamydia
867 trachomatis biovars reflect pathotype. 3. The Journal of infectious diseases 194:350357.
868 15. Liechti G, Kuru E, Packiam M, Hsu Y-P, Tekkam S, Hall E, Rittichier JT, VanNieuwenhze M, Brun
869 YV, Maurelli AT. 2014. Pathogenic Chlamydia Lack a Classical Sacculus but Synthesize a Narrow,

870 Mid-cell Peptidoglycan Ring, Regulated by MreB, for Cell Division. PLoS pathogens 12:e1005590.
871 16. Heddle JG, Barnard FM, Wentzell LM, Maxwell A. 2000. The interaction of drugs with DNA gyrase:
872 a model for the molecular basis of quinolone action. Nucleosides, Nucleotides & Nucleic Acids.
873 Taylor & Francis Group (Informa).
874 17. Grieshaber NA, Runac J, Turner S, Dean M, Appa C, Omsland A, Grieshaber SS. 2021. The
875 sRNA Regulated Protein DdbA Is Involved in Development and Maintenance of the Chlamydia
876 trachomatis EB Cell Form. 692224. Frontiers in Cellular and Infection Microbiology. Frontiers
877 Media S.A.
878 18. Lambden PR, Pickett MA, Clarke IN. 2006. The effect of penicillin on Chlamydia trachomatis DNA
879 replication. Pt 9. Microbiology (Reading, England) 152:25732578.
880 19. Hoare A, Timms P, Bavoil PM, Wilson DP. 2006. Spatial constraints within the chlamydial host cell
881 inclusion predict interrupted development and persistence. BMC microbiology 8:5.
882 20. Omsland A, Sager J, Nair V, Sturdevant DE, Hackstadt T. Developmental stage-specific metabolic
883 and transcriptional activity of Chlamydia trachomatis in an axenic medium. Proceedings of the
884 National Academy of Sciences of the United States of America 109:1978119785.
885 21. Abdelrahman Y, Ouellette SP, Belland RJ, Cox JV. 2016. Polarized Cell Division of Chlamydia
886 trachomatis. PLoS pathogens 12:e1005822.
887 22. Gregory WW, Gardner M, Byrne GI, Moulder JW. 1979. Arrays of hemispheric surface projections
888 on Chlamydia psittaci and Chlamydia trachomatis observed by scanning electron microscopy.
889 Journal of bacteriology 138:241244.
890 23. Matsumoto A. 1982. Surface projections of Chlamydia psittaci elementary bodies as revealed by
891 freeze-deep-etching. Journal of Bacteriology. American Society for Microbiology.
892 24. Nans A, Saibil HR, Hayward RD. 2014. Pathogen-host reorganization during Chlamydia invasion
893 revealed by cryo-electron tomography. Cellular Microbiology. Hindawi Publishing Corporation.
894 25. Liechti GW, Kuru E, Hall E, Kalinda A, Brun YV, VanNieuwenhze M, Maurelli AT. 2013. A new

895 metabolic cell-wall labelling method reveals peptidoglycan in Chlamydia trachomatis. Nature.
896 Springer Nature.
897 26. Ausmees N, Jacobs-Wagner C. 2000. Spatial and temporal control of differentiation and cell cycle
898 progression in Caulobacter crescentus. Annual review of microbiology 57:225247.
899 27. Lee K-C, Webb RI, Fuerst JA. 2009. The cell cycle of the planctomycete Gemmata obscuriglobus
900 with respect to cell compartmentalization. BMC cell biology 10:4.
901 28. Skerker JM, Laub MT. 2004. Cell-cycle progression and the generation of asymmetry in
902 Caulobacter crescentus. Nature Reviews Microbiology. Springer Nature.
903 29. Grieshaber S, Grieshaber N, Yang H, Baxter B, Hackstadt T, Omsland A. 2018. Impact of Active
904 Metabolism on Chlamydia trachomatis Elementary Body Transcript Profile and Infectivity. Journal
905 of Bacteriology. American Society for Microbiology.
906 30. Wang Y, Kahane S, Cutcliffe LT, Skilton RJ, Lambden PR, Clarke IN. 2011. Development of a
907 transformation system for Chlamydia trachomatis: restoration of glycogen biosynthesis by
908 acquisition of a plasmid shuttle vector. e1002258. PLoS Pathogens. Public Library of Science.
909 31. Chiarelli TJ, Grieshaber NA, Grieshaber SS. 2020. Live-Cell Forward Genetic Approach to Identify
910 and Isolate Developmental Mutants in Chlamydia trachomatis. JoVE. MyJoVE Corp.
911 32. Grieshaber NA, Chiarelli TJ, Appa CR, Neiswanger G, Peretti K, Grieshaber SS. 2022.
912 Translational gene expression control in Chlamydia trachomatis. e0257259. PLoS ONE. Public
913 Library of Science.
914 33. Edelstein AD, Tsuchida MA, Amodaj N, Pinkard H, Vale RD, Stuurman N. 2012. Advanced
915 methods of microscope control using Manager software. Journal of biological methods 1:10.

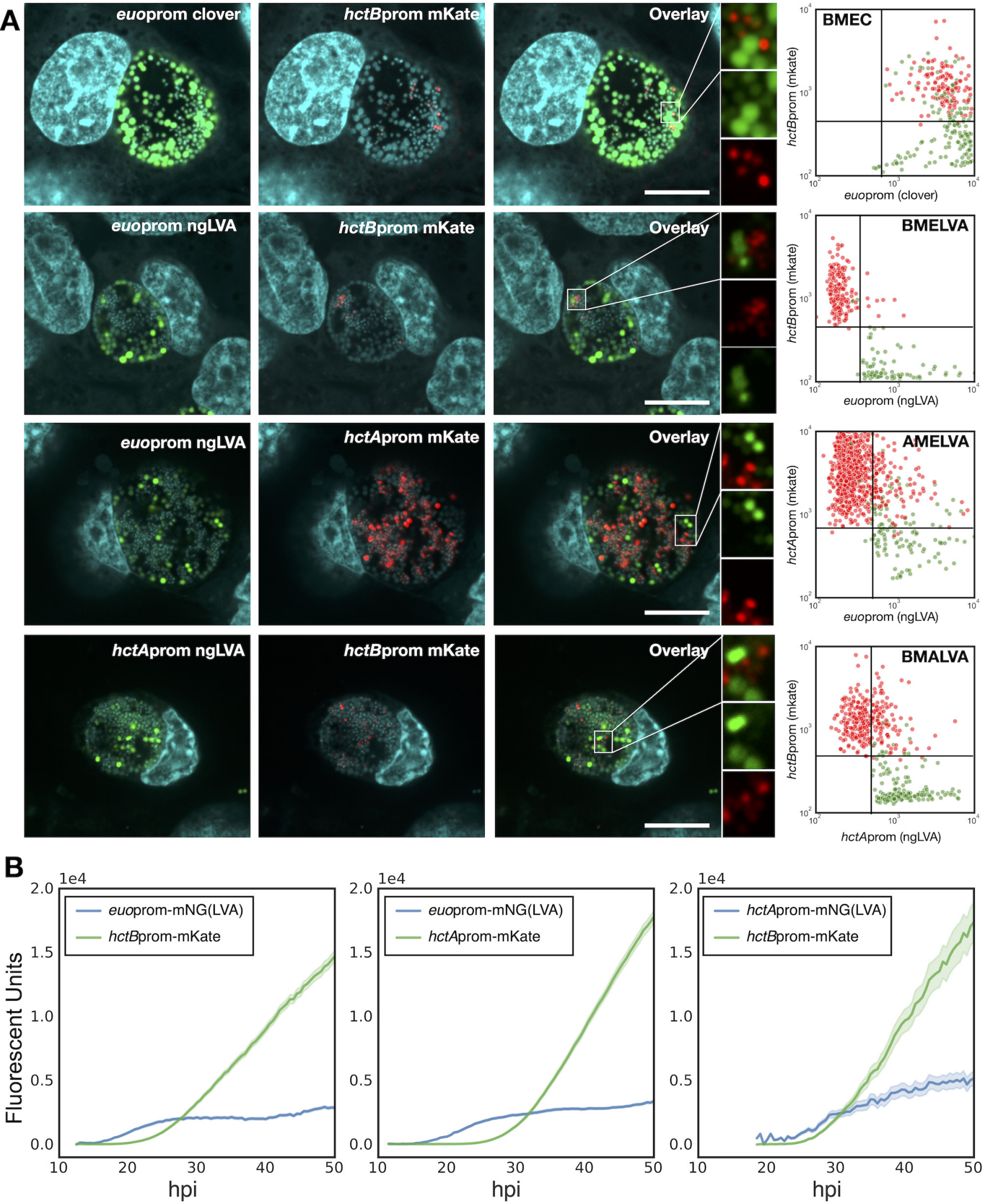
A
euoprom clover
hctBprom mKate
Overlay
BMEC
hctBprom (mkate)
euoprom (clover)
euoprom ngLVA
hctBprom mKate
Overlay
BMELVA
hctBprom (mkate)
euoprom (ngLVA)
euoprom ngLVA
hctAprom mKate
Overlay
AMELVA
hctAprom (mkate)
euoprom (ngLVA)
hctAprom ngLVA
hctBprom mKate
Overlay
BMALVA
hctBprom (mkate)
hctAprom (ngLVA)
B
1e4
Fluorescent Units
euoprom-mNG(LVA)
hctBprom-mKate
hpi
euoprom-mNG(LVA)
hctAprom-mKate
hpi
hctAprom-mNG(LVA)
hctBprom-mKate
hpi

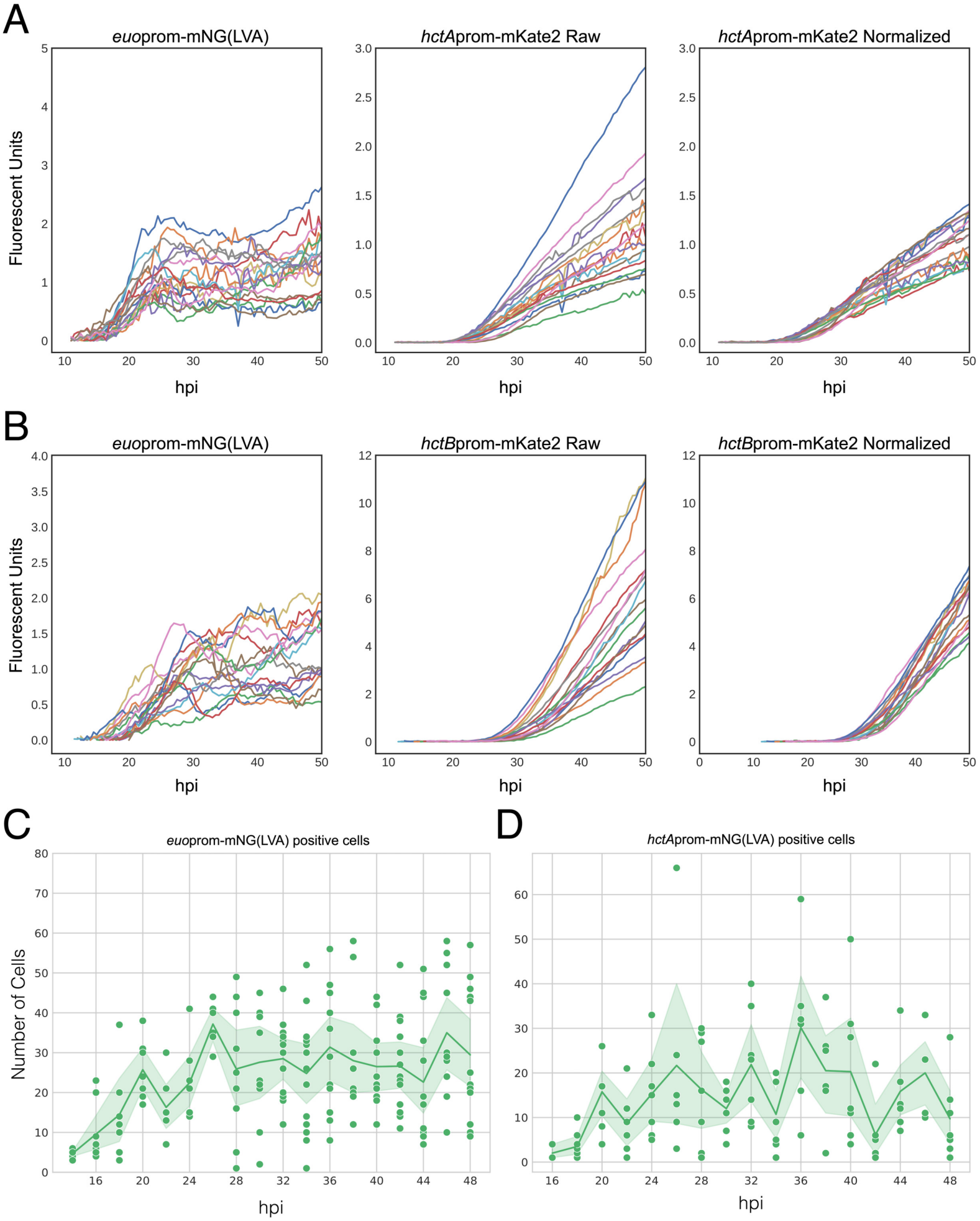
A
euoprom-mNG(LVA)
hctAprom-mKate2 Raw
hctAprom-mKate2 Normalized
Fluorescent Units
hpi
B
euoprom-mNG(LVA)
hctBprom-mKate2 Raw
hctBprom-mKate2 Normalized
Fluorescent Units
hpi
C
euoprom-mNG(LVA) positive cells
Number of Cells
hpi
D
hctAprom-mNG(LVA) positive cells
hpi

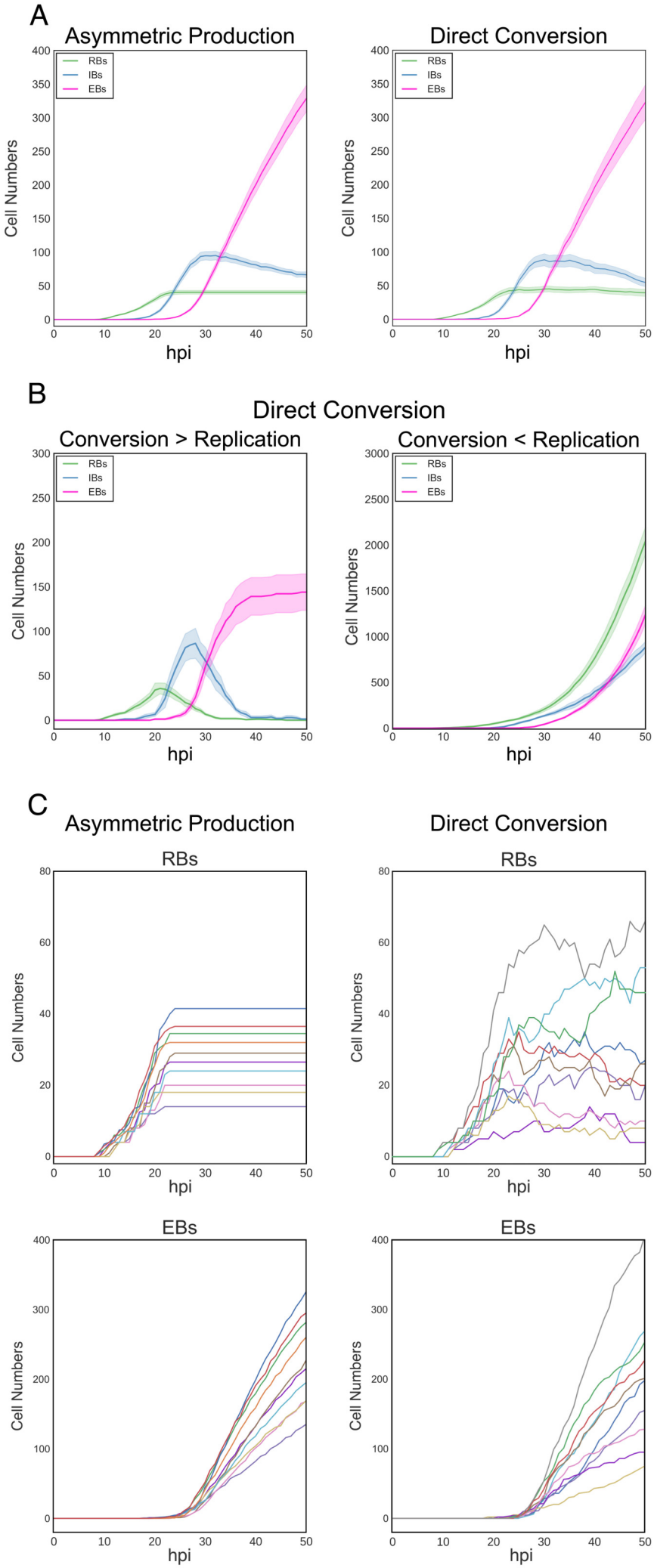
A
Asymmetric Production
Direct Conversion
RBs
IBs
EBs
Cell Numbers
hpi
B
Direct Conversion
Conversion > Replication
Conversion < Replication
C
Asymmetric Production
Direct Conversion
RBs
EBs

A

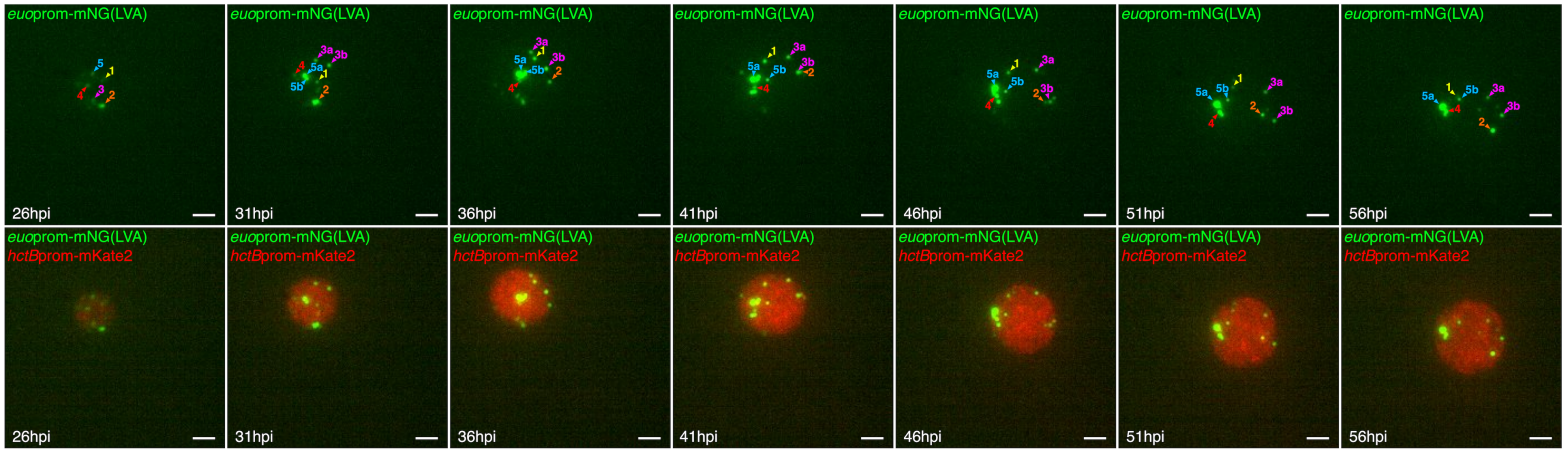
euoprom-mNG(LVA)
hctBprom-mKate2
26hpi
31hpi
36hpi
41hpi
46hpi
51hpi
56hpi

B

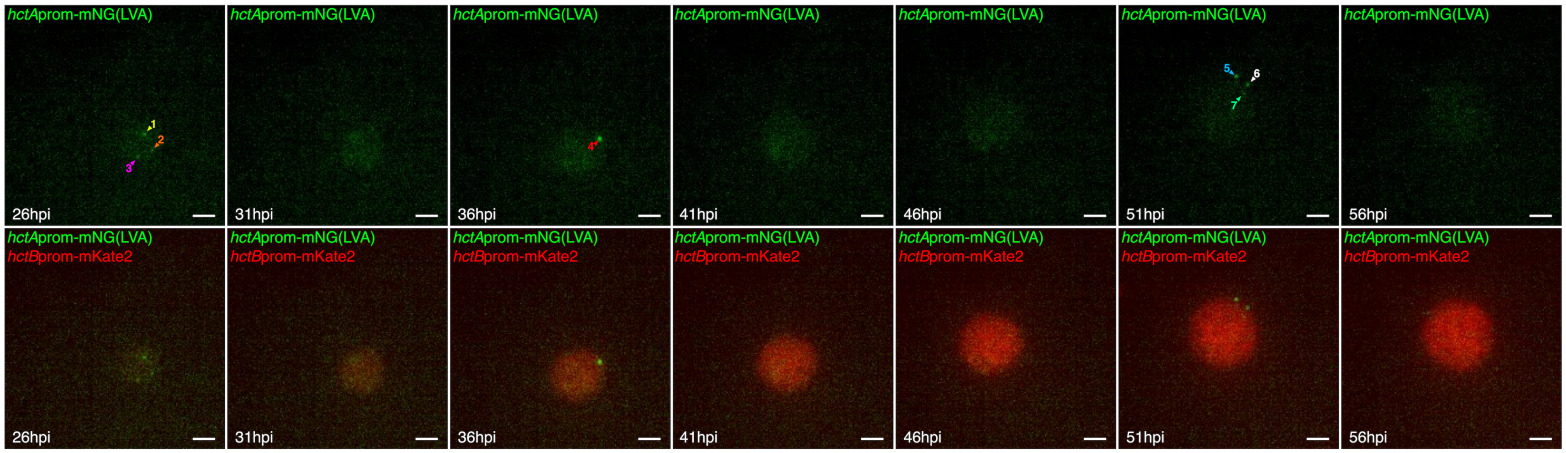
hctAprom-mNG(LVA)
hctBprom-mKate2
26hpi
31hpi
36hpi
41hpi
46hpi
51hpi
56hpi

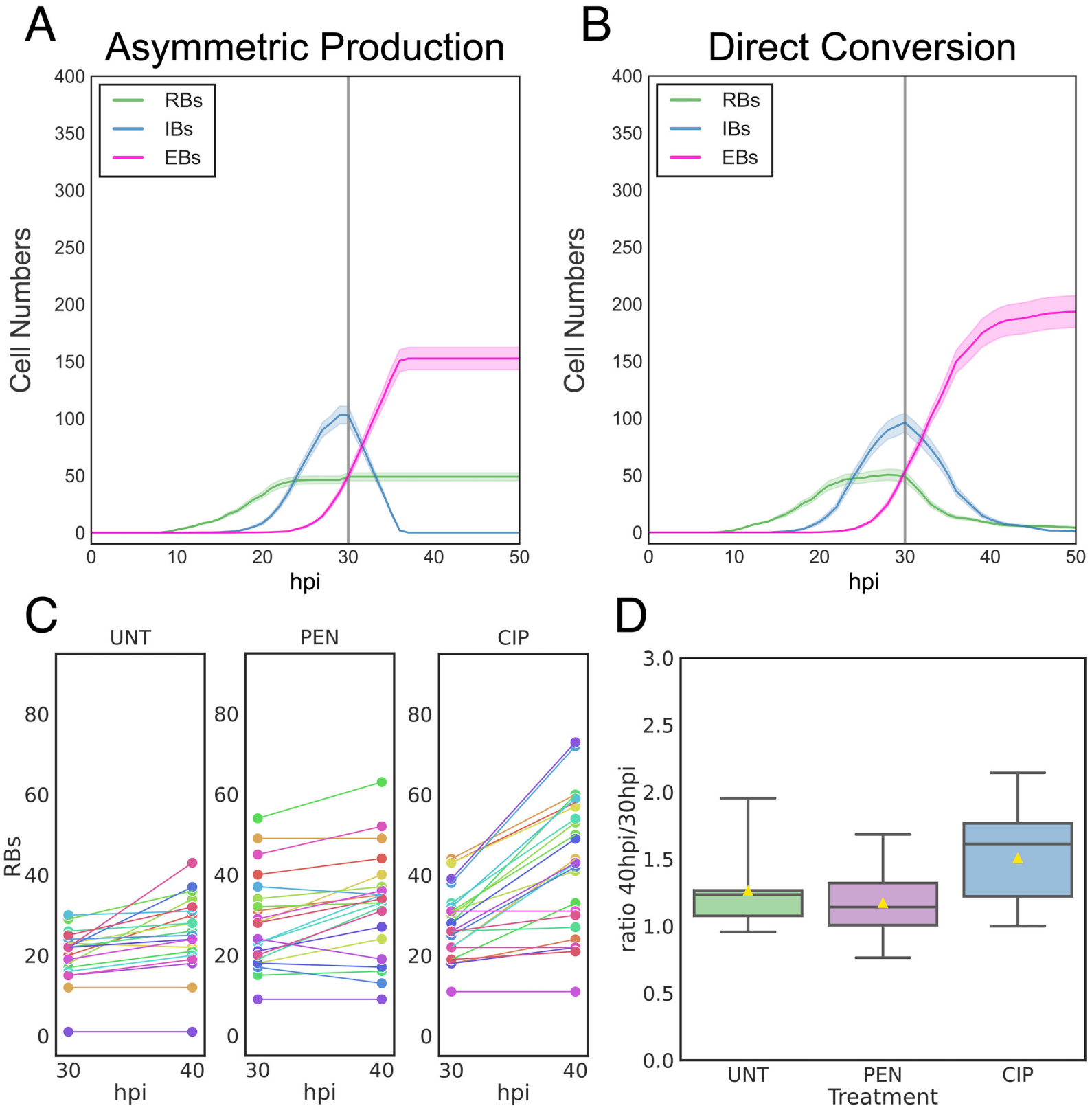
A
Asymmetric Production
RBs
IBs
EBs
Cell Numbers
hpi
B
Direct Conversion
RBs
IBs
EBs
Cell Numbers
hpi
C
UNT
PEN
CIP
RBs
hpi
D
ratio 40hpi/30hpi
UNT
PEN
CIP
Treatment

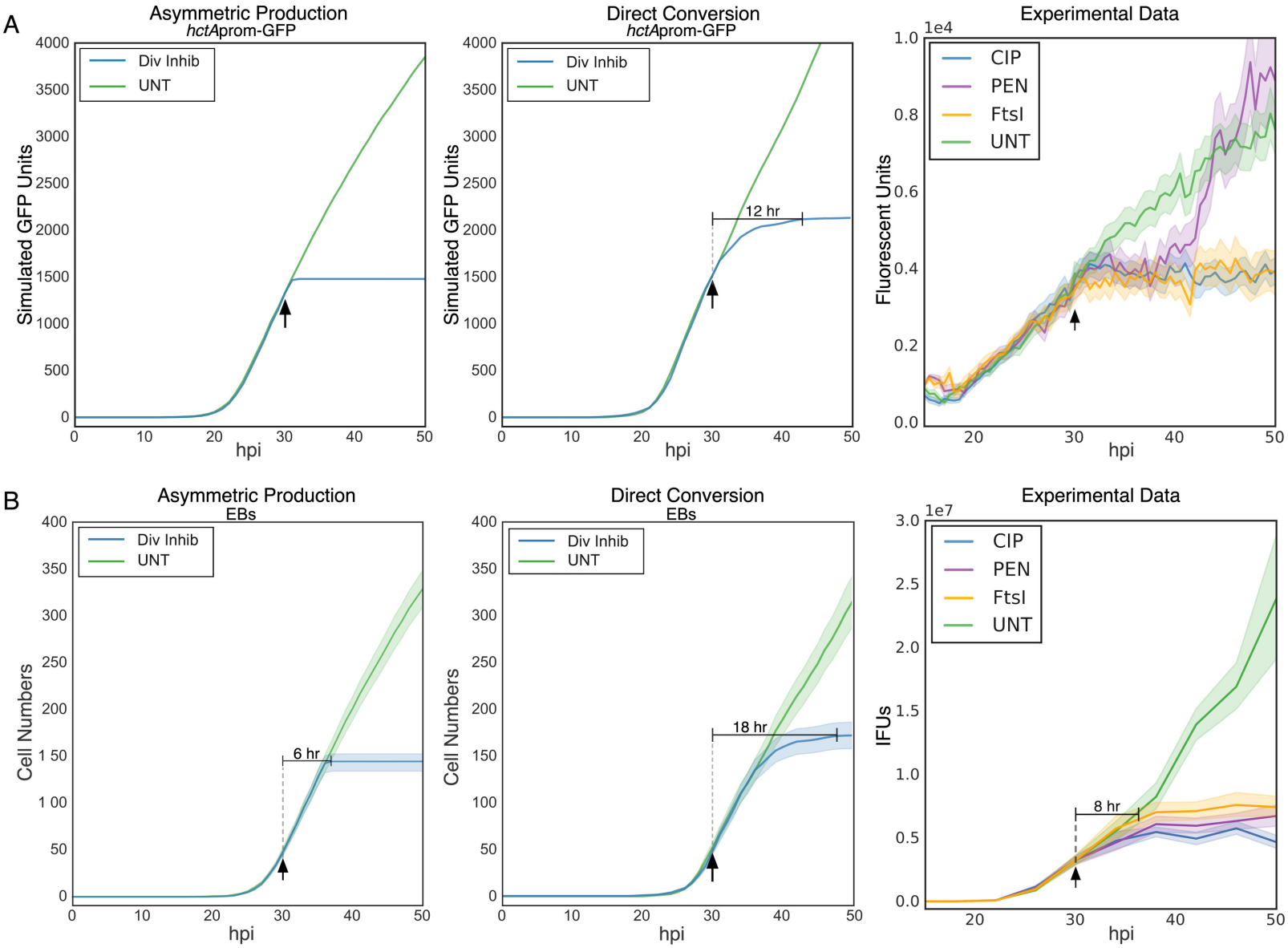
A
Asymmetric Production
hctAprom-GFP
Div Inhib
UNT
Simulated GFP Units
hpi
Direct Conversion
hctAprom-GFP
12 hr
Experimental Data
1e4
CIP
PEN
FtsI
UNT
Fluorescent Units
B
Asymmetric Production
EBs
6 hr
Cell Numbers
Direct Conversion
EBs
18 hr
Experimental Data
1e7
8 hr
IFUs

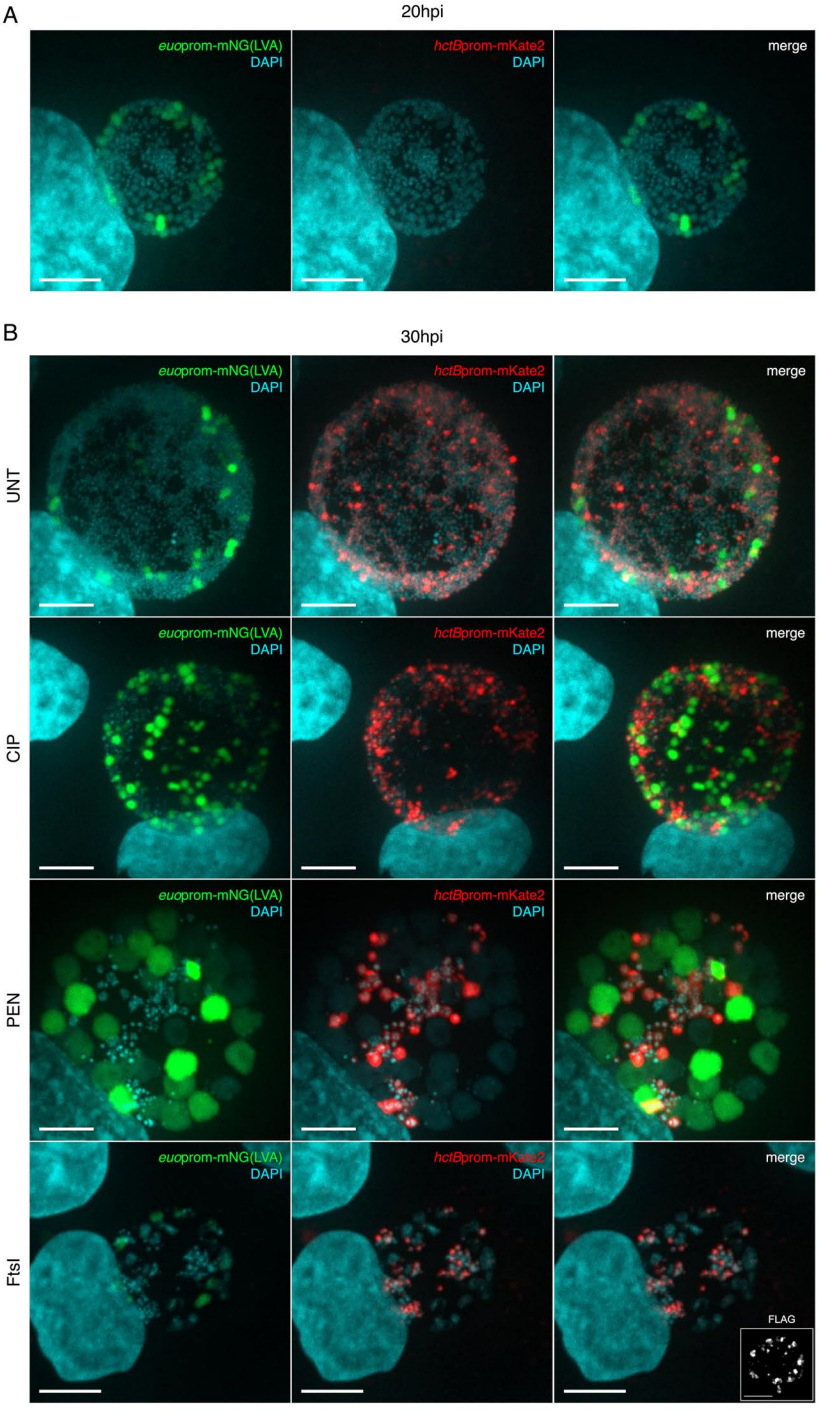
A
20hpi
euoprom-mNG(LVA)
DAPI
hctBprom-mKate2
DAPI
merge
B
30hpi
UNT
CIP
PEN
FtsI
FLAG

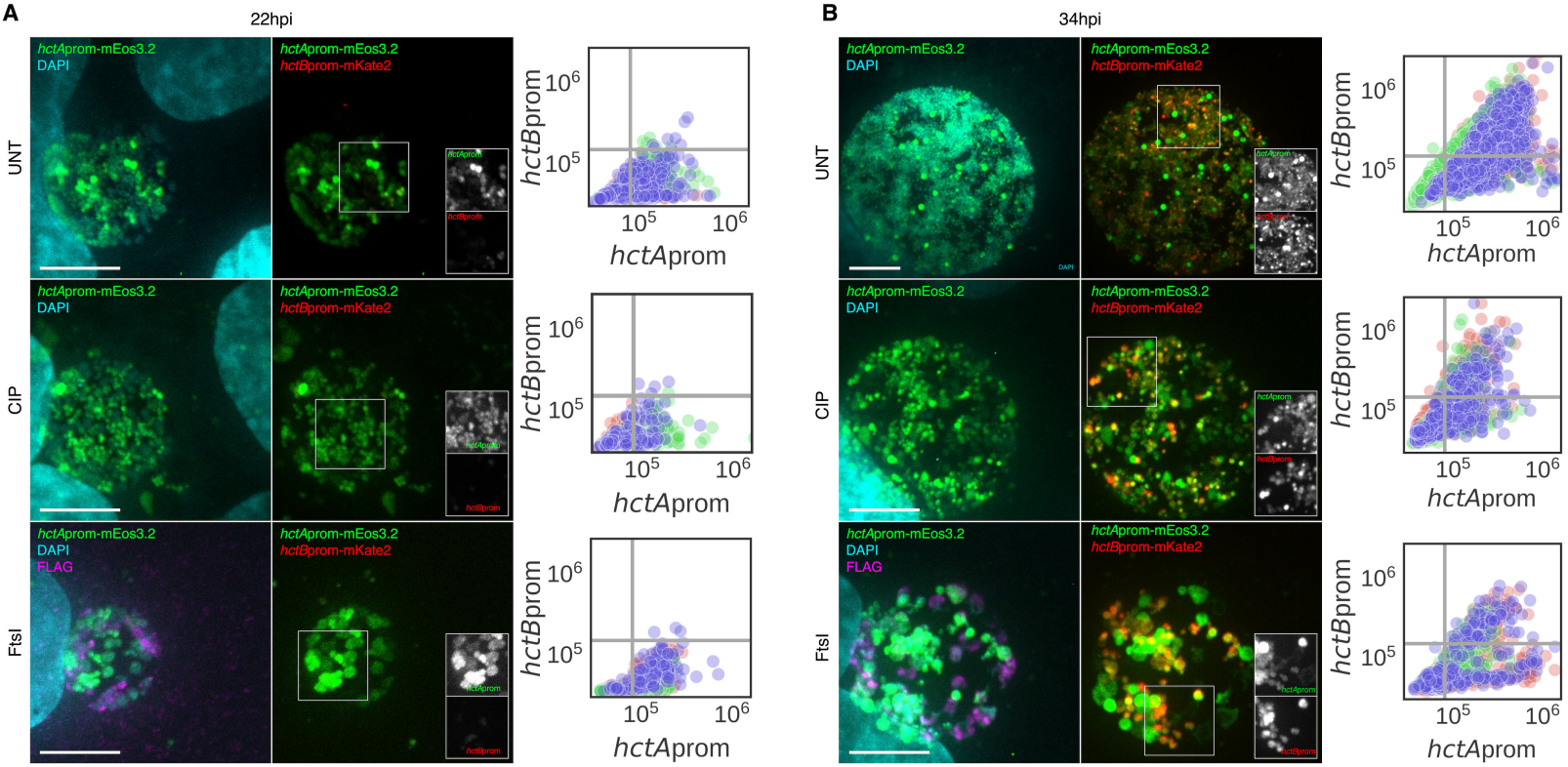
A
22hpi
B
34hpi
UNT
CIP
FtsI
hctAprom-mEos3.2
DAPI
hctBprom-mKate2
FLAG
hctBprom
hctAprom
10^5
10^6

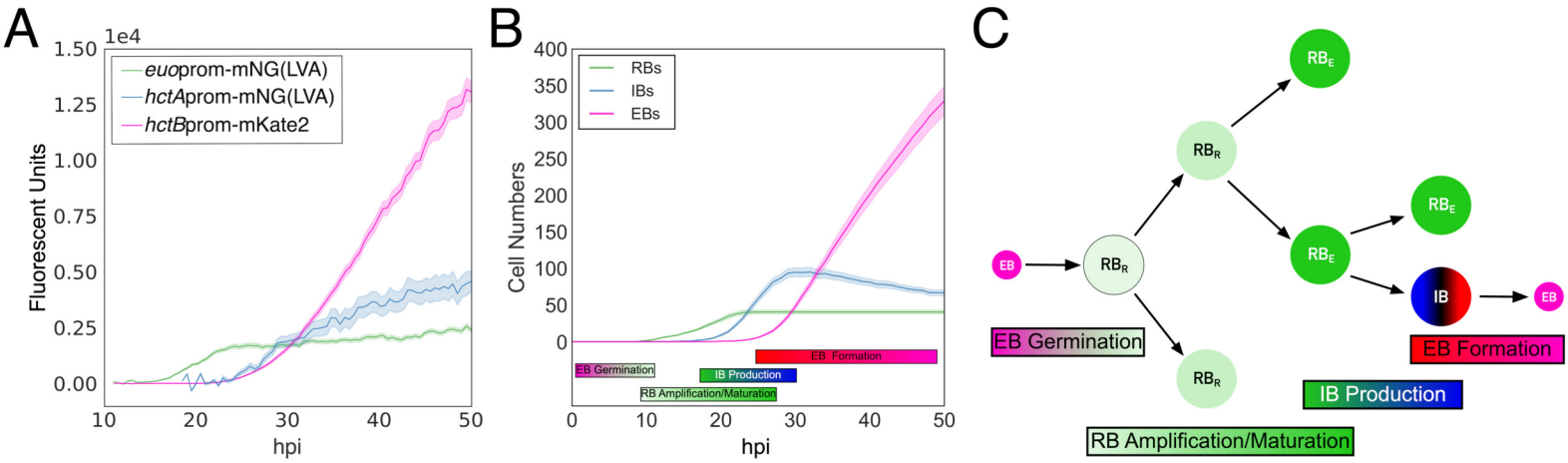
A
1e4
1.50
1.25
1.00
0.75
0.50
0.25
0.00
Fluorescent Units
euoprom-mNG(LVA)
hctAprom-mNG(LVA)
hctBprom-mKate2
10
20
30
40
50
hpi
B
400
350
300
250
200
150
100
50
0
Cell Numbers
RBs
IBs
EBs
EB Germination
IB Production
RB Amplification/Maturation
EB Formation
0
10
20
30
40
50
hpi
C
EB
RB_R
RB_E
IB
EB Germination
IB Production
RB Amplification/Maturation
EB Formation

Strain	Promoter F	Promoter F	Over expre	Cell type
L2-BMEC	hctBprom-	euoprom-clover		All cells (green), EBs (red)
L2-BMELV/	hctBprom-	euoprom-neongreen(L		RBs (green), EBs (red)
L2-AMELV/	hctAprom-	euoprom-neongreen(L		RBs (green), IBs (red)
L2-BMALV/	hctBprom-	hctAprom-neongreen(		IBs (green), EBs (red)
L2-BMAME	hctBprom-	hctAprom-mEos		IBs+EBs (green), EBs (red)
L2-E-FtsI-B	hctBprom-	hctAprom-	FtsI	IBs+EBs (green), EBs (red)
L2-E-ftsI-B	hctBprom-	euoprom-r	FtsI	RBs (green), EBs (red)

* Fluorescent half-life = 30 minutes